Economic Geology, v. XXX, no. XX, pp. X–X

Evolution of the Hydrothermal System Associated with the ABM Replacement-Style Volcanogenic Massive Sulfide Deposit, Finlayson Lake District, Yukon, Canada

Nikola Denisová † and Stephen J. Piercey

Department of Earth Sciences, Memorial University of Newfoundland, St. John's, Newfoundland A1B 3X5, Canada

Abstract

The ABM deposit, Finlayson Lake district, Yukon, Canada, is a bimodal-felsic, replacement-style volcanogenic massive sulfide (VMS) deposit (19.1 Mt @ 6.6 wt % Zn, 0.9 wt % Cu, 2.0 wt % Pb, 1.4 g/t Au, and 148 g/t Ag) hosted by Late Devonian continental back-arc–related volcanosedimentary rocks of the Kudz Ze Kayah formation. The VMS-related hydrothermal alteration associated with the deposit extends >1 km beyond the mineralization. Zones of pervasive sericite and chlorite alteration occur proximal to the massive sulfide lenses (<50 m) both in the hanging wall and the footwall, and zones of pervasive sericite and moderate sericite ± chlorite alteration extend laterally from the mineralization and into the hanging wall and footwall for hundreds to thousands of meters. Geochemical data and petrographic observations indicate that feldspar destruction and formation of white mica and chlorite were the main alteration processes. In both the hanging wall and footwall to the mineralization, base (e.g., Zn, Cu, Pb) and trace metals (e.g., Sb, Tl, Mo) form halos with elevated values up to 100 and 200 m, respectively.

The paragenesis and the formation conditions of the hydrothermal alteration were determined through petrography of hydrothermal alteration assemblages and their crosscutting relationships, electron microprobe analyses of the compositions of white mica, chlorite, and carbonate, and illite-chlorite geothermometry. These data suggest that the sericite ± chlorite assemblage was the earliest and most extensive phase of the hydrothermal alteration that formed at temperatures around 215° ± 30°C. Overprinting the sericite-chlorite assemblage is the pervasive sericite assemblage that formed at temperatures around 250° ± 15°C. The pervasive chlorite assemblage formed at temperatures around 320° ± 10°C and overprints the preceding sericite-rich assemblages. Microprobe analyses of white mica and chlorite generally show that Mg-rich varieties are more common proximal to mineralization and formed earlier in the deposit paragenesis than Fe-rich varieties. Mineralogy derived from short-wave infrared data for mica and chlorite, however, shows no clear spatial trends across the deposit due to complex overprinting relationships between alteration minerals.

Introduction

Hydrothermal alteration in volcanogenic massive sulfide (VMS) deposits reflects the interaction of upwelling fluids with footwall (and hanging-wall) lithofacies (Franklin et al., 1981). The nature of fluid-rock interactions is heavily influenced by the temperature and composition of both fluids and host rocks, the porosity and permeability of the deposit-hosting sequence, and subsequent postalteration overprinting from deformation and metamorphism (Franklin et al., 2005; Lafrance et al., 2020). In coherent volcanic flow-dominated sequences where fluids were interpreted to have exhaled on the sea floor, alteration commonly has distinct geometry, composition, and in many cases restricted distribution due to low permeability and porosity of the coherent host rocks (Riverin and Hodgson, 1980; Knuckey et al., 1983; Gemmell and Large, 1992; Gemmell and Fulton, 2001). In contrast, in sequences that are rich in volcaniclastic and sedimentary rocks and associated with subseafloor replacement, the alteration can be more complex due to the variability in permeable stratigraphy, which often results in more extensive interaction between the ascending hydrothermal fluids and host rocks, which in turn creates complex alteration geometries (Doyle and Allen, 2003; Franklin et al., 2005; Piercey, 2015).

Alteration processes cause geochemical and mineralogical changes in the host rocks and result in zoned geochemical and mineralogical alteration halos that surround VMS mineralization. Further, new and/or improved analytical methods have allowed for recent studies to test more subtle or previously undetectable hydrothermal alteration associated with VMS deposits (Yang et al., 2011; Genna and Gaboury, 2015; Buschette and Piercey, 2016; Soltani Dehnavi et al., 2018, 2019; Pilote et al., 2019; Brueckner et al., 2021). Despite an abundance of studies focusing on ancient VMS and modern-day sea-floor massive sulfide (SMS) deposits, understanding of the evolution of ancient hydrothermal systems and alteration footprints related to replacement-style VMS deposits in variously deformed and metamorphosed sequences is incomplete.

The Finlayson Lake district in southeastern Yukon, Canada, hosts >40 Mt of polymetallic VMS mineralization in six deposits (Kona, ABM, GP4F, R15, Wolverine, and Ice) within arc and back-arc rocks of the Yukon-Tanana and Slide Mountain terranes (Peter et al., 2007). The ABM deposit is a bimodal-felsic, replacement-style VMS deposit and contains a total (geologic) mineral resource of 19.1 Mt @ 6.6 wt % Zn, 0.9 wt % Cu, 2.0 wt % Pb, 1.4 g/t Au, and 148 g/t Ag (van Olden et al., 2020). In 2015, drilling at the ABM deposit discovered a new mineralized zone (Krakatoa zone), which contributed to the reinterpretation of the mineralization as replacement-style (van Olden et al., 2020). Despite the new interpreta-

†Corresponding author: e-mail, ndenisova@mun.ca

ISSN 0361-0128; doi:10.5382/econgeo.5004; 29 p.
Digital appendices are available in the online Supplements section.

Submitted: June 7, 2022/Accepted: October 27, 2022

tions, there has been little documentation of the hydrothermal alteration and its relationship to replacement. Further, the relatively low degree of metamorphism and deformation (greenschist facies predominantly) at the ABM deposit makes it ideal for studying the evolution of a hydrothermal system associated with an ancient replacement-style VMS deposit in a back-arc environment, as numerous workers have shown that greenschist metamorphism does not significantly affect the geochemical and mineral-chemical signatures produced by hydrothermal alteration and that recrystallized alteration-related phyllosilicates preserve their original premetamorphic compositions (Riverin and Hodgson, 1980; Urabe et al., 1983; Hannington et al., 2003; Genna and Gaboury, 2015).

Considering the above, this study utilizes detailed alteration mineral assemblage observations, whole-rock geochemistry, alteration mineral chemistry, and short-wave infrared spectroscopy (SWIR) methods to provide a descriptive and genetic framework for hydrothermal alteration in the ABM replacement-style VMS deposit. The relationships between the different alteration assemblages are used to interpret the temporal and spatial evolution of the hydrothermal system and the geochemical and mineralogical footprint associated with the formation of the ABM deposit. Our research will provide insight into processes active in subseafloor replacement in VMS deposits and into geochemical and mineralogical vectors toward mineralization and the hydrothermal footprint of VMS deposits. This has implications not only for VMS exploration in the Finlayson Lake district, but also for the study and exploration of replacement-style VMS deposits in similar environments around the world.

Regional Geology

The Finlayson Lake district is a dismembered block of the Yukon-Tanana and Slide Mountain terranes that developed along the western margin of Laurentia throughout the mid-Paleozoic to the Permo-Triassic (Fig. 1; Colpron et al., 2006; Nelson et al., 2006; Piercey et al., 2006). In the Eocene, it was displaced from its original location approximately 430 km along the dextral strike-slip Tintina fault (Gabrielse et al., 2006). The Yukon-Tanana terrane comprises a polydeformed and metamorphosed pre-Late Devonian continental margin assemblage (Snowcap assemblage; Piercey and Colpron, 2009) that is overlain by three unconformity-bound Late Devonian to Middle to Late Permian continental arc, back-arc, and ocean basin-related volcanosedimentary sequences (Big Campbell, Money Creek, and Cleaver Lake thrust sheets; Mortensen and Jilson, 1985; Mortensen, 1992; Colpron et al., 2006; Murphy et al., 2006). The core of the Finlayson Lake district reached amphibolite facies metamorphic grade, which transitions to lower greenschist facies farther from the center of the district (Murphy et al., 2006). The Big Campbell thrust sheet is by volume the largest and structurally deepest of structural blocks in the Finlayson Lake district (Fig. 1). It consists of Upper Devonian metaclastic rocks of the North River formation, the Upper Devonian Grass Lakes group, and the Lower Mississippian Wolverine Lake group, and hosts five VMS deposits (Fig. 1; Murphy et al., 2006; Peter et al., 2007). The Grass Lakes group comprises three units: the Fire Lake, Kudz Ze Kayah, and Wind Lake formations (Fig. 1). The Fire Lake formation hosts the Kona Cu-Co-Au VMS deposit within mafic metavolcanic and lesser amounts of mafic and ultramafic metasubvolcanic rocks (Piercey et al., 2001a; Sebert et al., 2004; Murphy et al., 2006; Peter et al., 2007). The Kudz Ze Kayah formation formed in a continental back-arc setting juxtaposed adjacent to the Fire Lake formation (Manor et al., 2022a) and hosts the ABM, GP4F, and R15 deposits. It comprises dominantly felsic volcanic and sedimentary rocks with back-arc geochemical affinities (Piercey et al., 2001b; Murphy et al., 2006; Manor et al., 2022a, b). The Wind Lake formation is conformable atop the Kudz Ze Kayah formation and consists of interlayered carbonaceous sedimentary rocks and alkalic mafic volcanic rocks (Piercey et al., 2002). All rocks in the Grass Lakes group are intruded by the Grass Lakes plutonic suite at ca. 361 Ma (Piercey et al., 2001b; 2003; Manor et al., 2022b). The Wolverine Lake group unconformably overlies the Grass Lakes group and contains basal conglomerates, sandstones, felsic volcanic rocks, carbonaceous phyllites/shales, iron formations, and basaltic rocks, which host the Wolverine felsic-siliciclastic–type VMS deposit (Murphy and Piercey, 1998; Bradshaw et al., 2001, 2008).

The Kudz Ze Kayah formation hosts three known VMS deposits: the ABM deposit, the GP4F deposit, and the R15 deposit. They are located about 25 km south of Finlayson Lake and the Robert Campbell Highway (Fig. 1). The GP4F deposit (Boulton, 2002) is situated roughly 5 km southeast from the ABM deposit (Fig. 1) and sits ~500 to 600 m stratigraphically below the ABM deposit (Peter et al., 2007; Manor et al., 2022b). The R15 deposit occurs immediately along strike east of the GP4F deposit and occupies the same stratigraphic position (MacRobbie and Holroyd, unpub. data). The ABM deposit sits roughly 150 to 250 m below the contact between the Kudz Ze Kayah and Wind Lake formations (Manor et al., 2022b). Subseafloor replacement is interpreted to be the primary mineralization style in all deposits (Peter et al., 2007; van Olden et al., 2020; Denisová and Piercey, 2022; Manor et al., 2022b). The formation of rocks hosting the GP4F deposit was dated at ca. 363.254 ± 0.098 Ma, whereas the ABM deposit is hosted by rocks dated at ca. 362.82 ± 0.12 Ma (Manor et al., 2022b). The volcanic activity responsible for the deposition of the entire Kudz Ze Kayah formation is interpreted to have lasted approximately 0.65 to 1.0 m.y., indicating that rapid deposition and emplacement of volcanosedimentary rocks played an important role in the formation of both VMS deposits (Manor et al., 2022b).

Local Geology

The rocks of the Kudz Ze Kayah formation have been interpreted to have formed in a back-arc environment based on their geochemical signatures and tectonostratigraphic setting (Piercey et al., 2001b; 2002). The upper Kudz Ze Kayah formation, which hosts the ABM deposit in the top ~350 m, is interpreted to have been deposited in an actively extending basin (Denisová and Piercey, 2022; Manor et al., 2022b), and the volcanosedimentary package consists of abundant felsic volcaniclastic and coherent rocks and lesser mafic sills and argillite lenses. The stratigraphy dips between 20° and 30° to the north-northeast, and field observations and stratigraphic reconstructions do not indicate any fault repetition or major folding (van Olden et al., 2020; Denisová and Piercey, 2022; Manor et al., 2022b). The distribution of abundant coherent

felsic facies (e.g., sills, flows, domes) and mafic sills, together with abundant volcaniclastic rocks that are typically proximal to active volcanic sites (crystal-rich tuffs, lapilli tuffs), suggests that the ABM deposit formed at the site of an active volcanic center (Denisová and Piercey, 2022). Denisová and Piercey (2022) also note that the East fault (Fig. 2), previously interpreted to be a reactivated transform fault (van Olden et al., 2020), was originally a part of a set of interconnected synvolcanic normal faults. The synvolcanic faults accommodated the subsidence in the back-arc basin, served as conduits for ascending magmas, controlled the emplacement of coherent volcanic units and locally the thickness of volcaniclastic and sedimentary units, and were important in controlling the upwelling VMS-related hydrothermal fluids (Fig. 2).

The upper Kudz Ze Kayah formation can be divided into three distinct sequences with different geochemical characteristics, Sequence 1 being the stratigraphically lowest and Sequence 3 being the stratigraphically highest. Sequence 1 consists of felsic volcaniclastic rocks, sills, and rare argillite lenses. Sequence 2 hosts the massive sulfide mineralization and comprises felsic volcaniclastic rocks, coherent flows, sills, domes, and two mafic sills that extend through the deposit footprint. Sequence 3 contains abundant felsic volcaniclastic rocks, felsic flows and sills, and argillite lenses. The boundary between Sequence 2 and Sequence 3 consists of an extensive argillite lens that marks a protracted period of volcanic quiescence. Other, lesser argillite lenses in its hanging wall mark later minor breaks in volcanism during the deposition of Sequence 3.

Mineralization at the ABM Deposit

The ABM deposit consists of two mineralized zones: the ABM zone and the Krakatoa zone (Fig. 2), that were offset along the East fault postmineralization. The mineralization in each zone consists of a series of stacked, stratabound massive sulfide lenses enveloped by pervasive alteration that dip subparallel to the stratigraphy (20°–30°; Fig. 3). The ABM zone is 700 m wide and extends from the bedrock surface downdip for 600 m. Mineralization in the ABM zone tapers off downdip to the north-northeast, along strike to the west, and is cut off by the East fault. The Krakatoa zone is 170 m wide and extends from the bedrock surface downdip for 600 m and remains open downdip, whereas along strike, the mineralized lenses are cut off by postmineralization faults.

In both the ABM and Krakatoa zones, three main ore assemblages compose the massive sulfide lenses (Denisová and Piercey, 2022): (1) a pyrite-sphalerite-galena ± chalcopyrite-tetrahedrite group sulfosalts assemblage with common associated carbonate, barite, quartz, and white mica; (2) an assemblage comprising pyrite-chalcopyrite-pyrrhotite-magnetite-sphalerite ± galena-tetrahedrite group sulfosalts, with minor associated carbonate and chlorite that occurs commonly in the core of the sulfide lenses; (3) chalcopyrite-pyrrhotite-pyrite stringers associated with pervasive chlorite alteration, with minor associated carbonate, and quartz. The massive sulfide lenses are primarily composed of the first two assemblages. The third assemblage is not as common and typically only present at the upper and lower contacts of the massive sulfide lenses.

In the ABM zone, massive sulfide mineralization is associated with felsic volcanic and volcaniclastic rocks. In the Krakatoa zone, most of the massive sulfide mineralization is localized on mafic sill contacts or within the mafic sills themselves. In recent years, the ABM deposit has been reinterpreted as a replacement-style VMS deposit (van Olden et al., 2020; Denisová and Piercey, 2022; Manor et al., 2022b). Features such as preserved lapilli and other clasts, remnant bedding, and massive sulfides replacing glassy groundmass within perlitic and brecciated textures on unit contacts occur within the massive sulfide lenses and on their contacts and suggest that the mineralization formed by replacement (Doyle and Allen, 2003).

Methods

This study builds on the work presented in Denisová and Piercey (2022); the same sample set is used to describe and investigate the hydrothermal system at the ABM deposit; the existing lithogeochemical data set was extended beyond immobile elements to supplement them with mobile elements acquired using different digestions and analytical methods. Graphic logging was performed for ~10 km of drill core from 51 drill holes and recorded lithology, primary textures, grain size, mineralogy, and alteration type and intensity based on mineral occurrence (quartz, sericite, chlorite, biotite, carbonates, and sulfides). Out of 478 collected samples, 83 were analyzed for lithogeochemistry to characterize the host rocks and alteration, and 82 representative samples were studied petrographically. In addition, alteration minerals and their paragenesis were studied in 51 samples representing main types of mineralization. Petrography was undertaken using standard petrographic microscopy and a JEOL JSM 7100F scanning electron microscope (SEM) at Memorial University using backscattered electron (BSE) imaging operating at an accelerated voltage of 15 kV. Data sets provided by BMC Minerals Ltd., including core photos, drill logs, and geochemical data, were used as additional resources to document the macroscale alteration in the deposit; the quality assurance and quality control procedures for the company analytical data sets are described in van Olden et al. (2020). Presented cross sections displaying modeled alteration zones are based primarily on detailed graphic drill logs; company drill logs and drill core photos were used to populate gaps between the acquired data and to refine the model. All models and interpretations carry a higher degree of uncertainty in the footwall of the mineralization due to limited drilling below the ore horizon. Digital models of alteration zones and mineralized lenses were created using the Leapfrog Geo 6.0 software developed by Seequent. Isosurfaces of Ba distribution (Figs. 2, 4) were modeled using the Numeric Models tool in Leapfrog 3D. The linear radial basis function (RBF) interpolation was chosen to mitigate the irregular distribution of the almost 9,000 Ba data points from the assay database of BMC Minerals Ltd. The linear RBF interpolant was run with a sill value of 5,000, base range of 50, nugget of 0, and accuracy of 20. The trend was set to the local stratigraphy (dip 30° with dip azimuth of 20° and pitch of 115°), and the ellipsoid ratios were set to 3:3:1. The threshold value for Ba at the deposit was chosen at 3,500 ppm using methods outlined in Reimann et al. (2005). Throughout this study, we will refer to micaceous material observed in drill core and hand samples as sericite due to its relatively fine grain size and ubiquity. The term white mica will be used for colorless

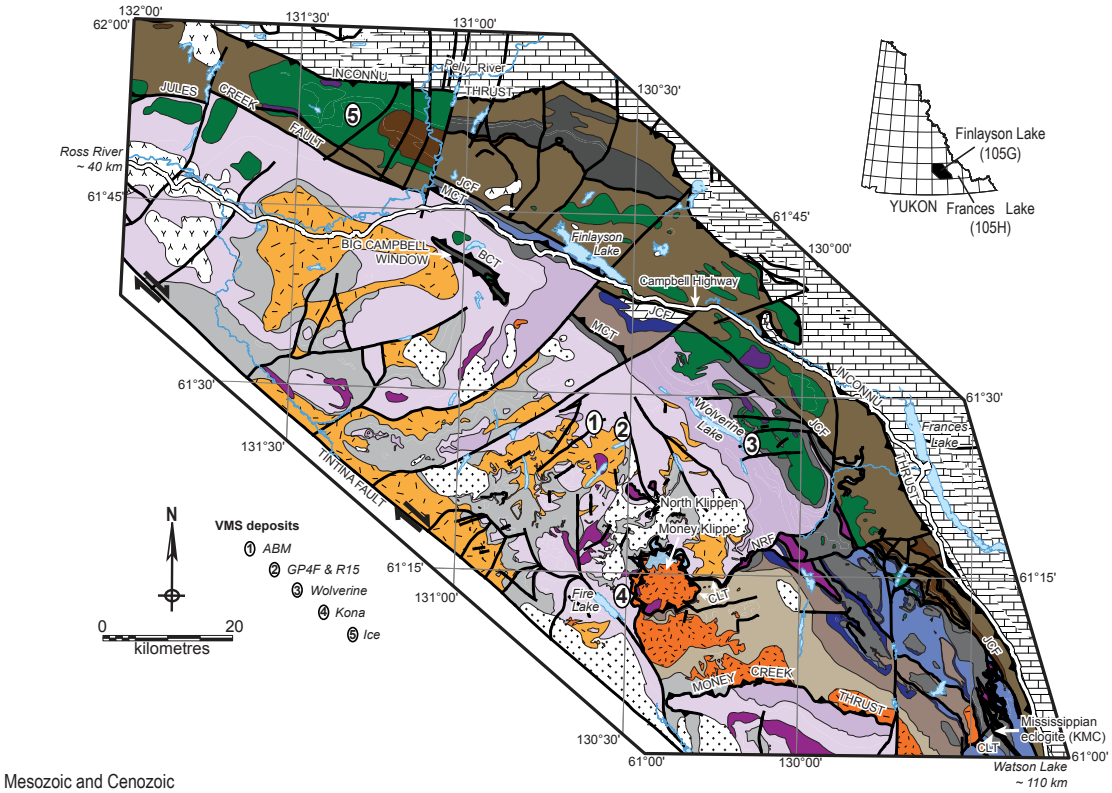

Mesozoic and Cenozoic

undifferentiated intrusions

undifferentiated volcanic rocks

North American Continental Margin

Triassic

dark shale, siltstone and limestone

Paleozoic

undifferentiated formations of Selwyn Basin, Cassiar/McEvoy Platform, Earn Group and Mt. Christie Formation

Post - YTT / SMT Amalgamation

Triassic

grey shale, siltstone and limestone

Permian - Triassic

SIMPSON LAKE GROUP

polymictic conglomerate, sandstone, siltstone, mafic and felsic volcanic rocks, limestone

Slide Mountain terrane

INTRUSIVE ROCKS

Early Permian

ultramafic and mafic intrusions

LAYERED ROCKS

Lower to Middle Permian

Gatehouse formation

limestone and quartzite

Slide Mountain terrane (SMT)

Lower Permian

Campbell Range formation

basalt and varicoloured chert

Carboniferous to Permian?

FORTIN CREEK GROUP

dark phyllite and chert, varicoloured chert, chert-pebble conglomerate, sandstone, limestone, felsic and mafic metavolcanic rocks

Yukon-Tanana terrane

INTRUSIVE ROCKS

Early Mississippian

SIMPSON RANGE PLUTONIC SUITE

granite, quartz monzonite, granodiorite

Late Devonian to Early Mississippian

GRASS LAKES PLUTONIC SUITE

granite, quartz monzonite augen granite

ultramafic and mafic rocks, Big Campbell and Cleaver Lake thrust sheets

LAYERED ROCKS

Lower Permian

Money Creek formation

dark phyllite and sandstone, chert, chert-pebble conglomerate, diamictite

Mid-Pennsylvanian to Lower Permian

Finlayson Creek limestone

massive bioclastic limestone

Yukon-Tanana terrane (YTT)

Upper Mississippian to mid-Pennsylvanian

undifferentiated White Lake and King Arctic formations

green and pink chert, limestone, sandstone, conglomerate, mafic metavolcanic rocks

Upper Mississippian

Whitefish limestone

massive bioclastic limestone

Lower Mississippian

Tuchitua River formation

intermediate, felsic and mafic volcanic rocks, sandstone, chert, limestone

WOLVERINE LAKE GROUP

undifferentiated mafic and felsic volcanic rocks and dark clastic rocks

Upper Devonian to Lower Mississippian

Cleaver Lake formation

calc-alkaline basalt, rhyolite, chert and volcanic-derived sandstone

Waters Creek formation

felsic to intermediate metavolcanic rocks and carbonaceous phyllite

GRASS LAKES GROUP

undifferentiated mafic and felsic volcanic rocks and dark clastic rocks of the Fire Lake, Kudz Ze Kayah and Wind Lake formations

Pre-Upper Devonian

North River formation

quartzose metaclastic rocks, marble and non-carbonaceous pelitic schist

Fig. 1. Regional setting of the Finlayson Lake district. A) Regional geologic map of the Finlayson Lake district, Yukon-Tanana, and Slide Mountain terranes (modified after Murphy et al., 2006). Numbers mark the positions of known volcanogenic massive sulfide (VMS) deposits in the region. Abbreviations: BCT = Big Campbell thrust, CLT = Cleaver Lake thrust, JCF = Jules Creek fault, MCT = Money Creek thrust, NRF = North River thrust. B) Composite chronostratigraphic column for the Finlayson Lake district showing stratigraphic and structural relationships. Locations of VMS deposits, petrogenetic affinities of volcanic rocks and U-Pb and fossil ages displayed on diagram (modified after Murphy et al., 2006; Piercey et al., 2016; Manor and Piercey, 2018).

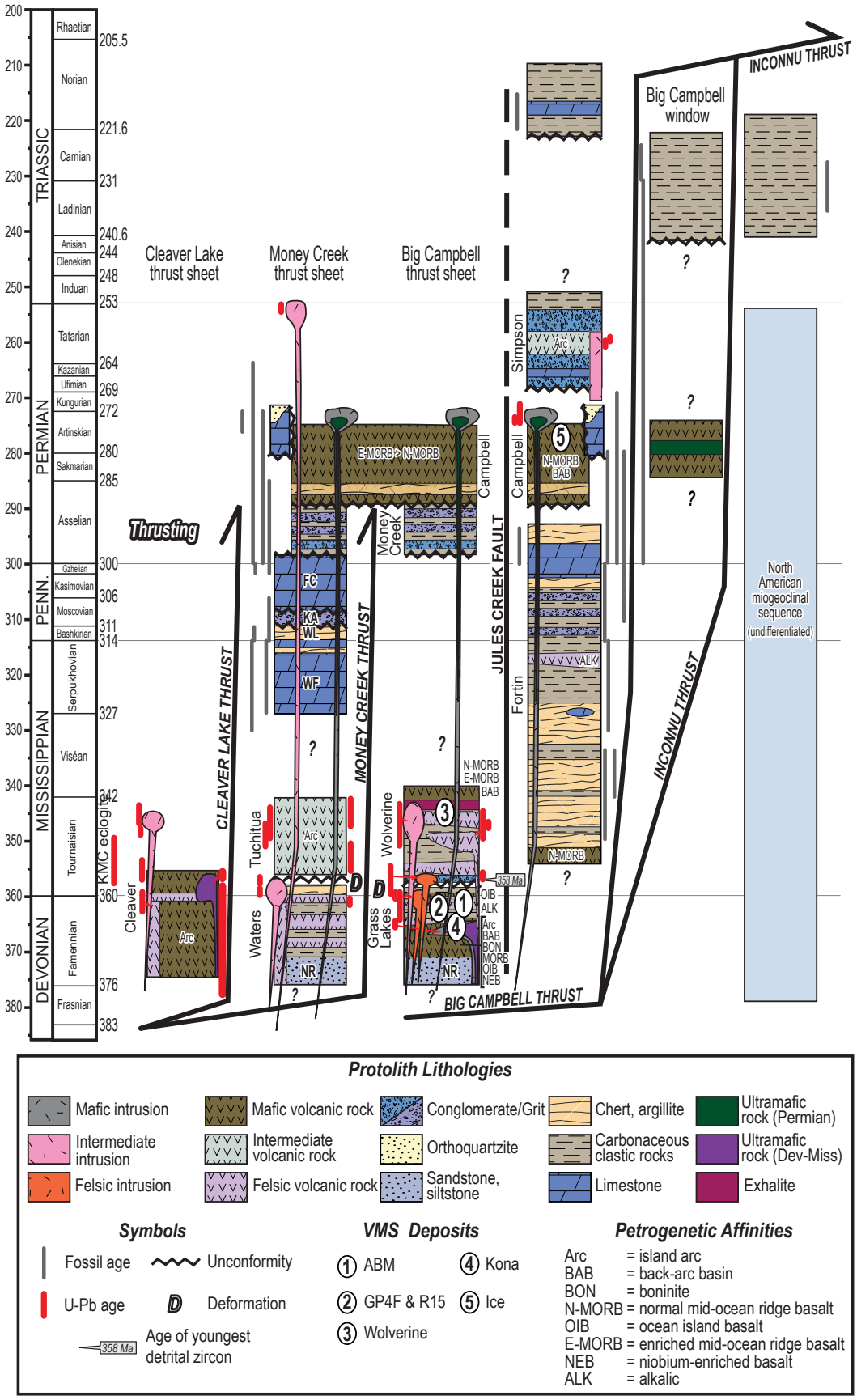

Fig. 1. (*Cont.*)

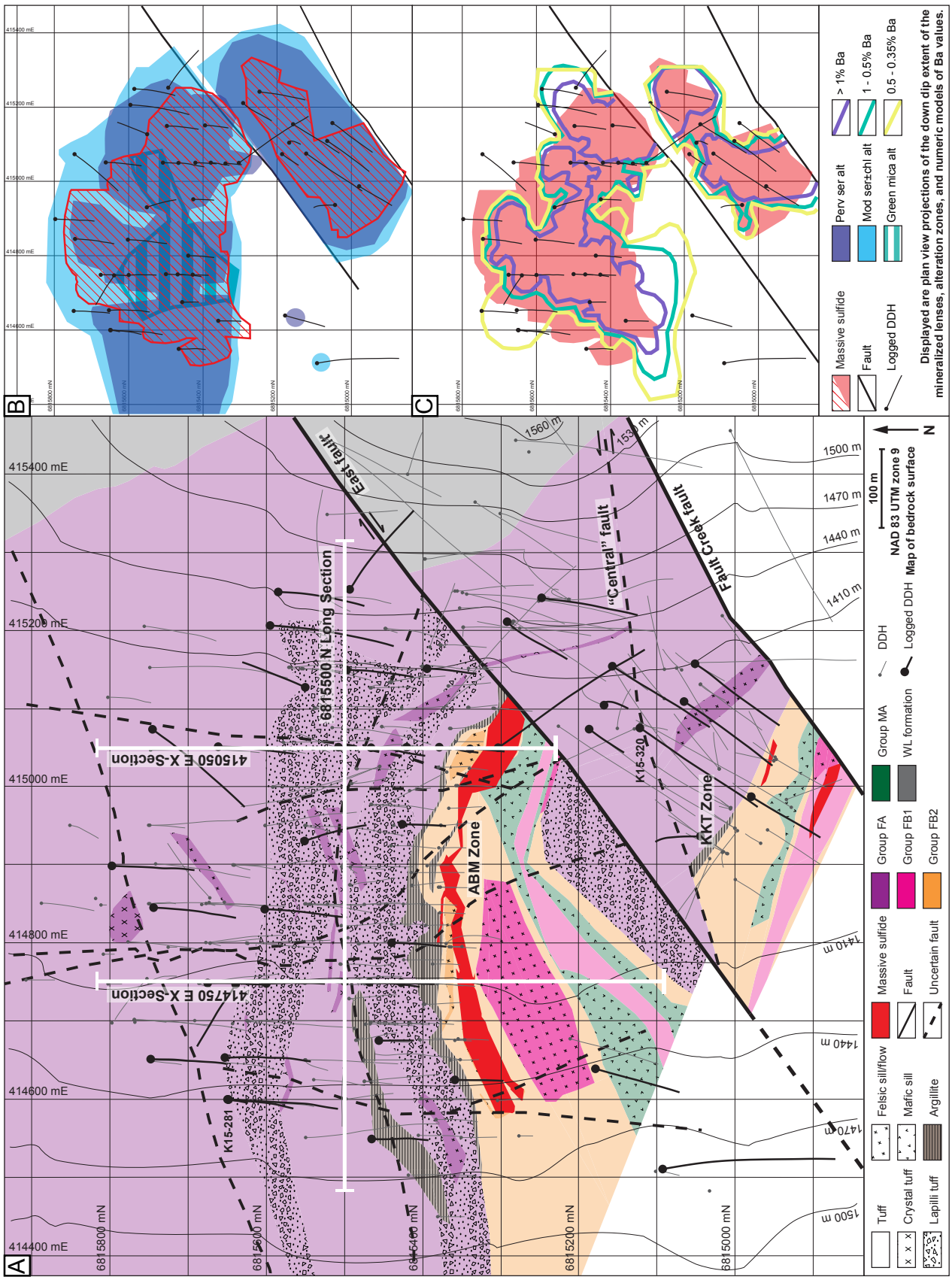

Fig. 2. Local geology of the ABM deposit. A) Geologic map with units constructed using drilling data and 3-D models. Cross section and long section lines displayed. Note that lithofacies are displayed using patterns and geochemical groups using colors. B) Upward projections of maximum extent of modeled alteration zones and mineralization. C) Upward projection of mineralization and maximum extent of numerically modeled Ba isosurfaces. Abbreviations: chl = chlorite, DDH = diamond drill hole, FA = felsic A, FB = felsic B, MA = mafic A, ser = sericite

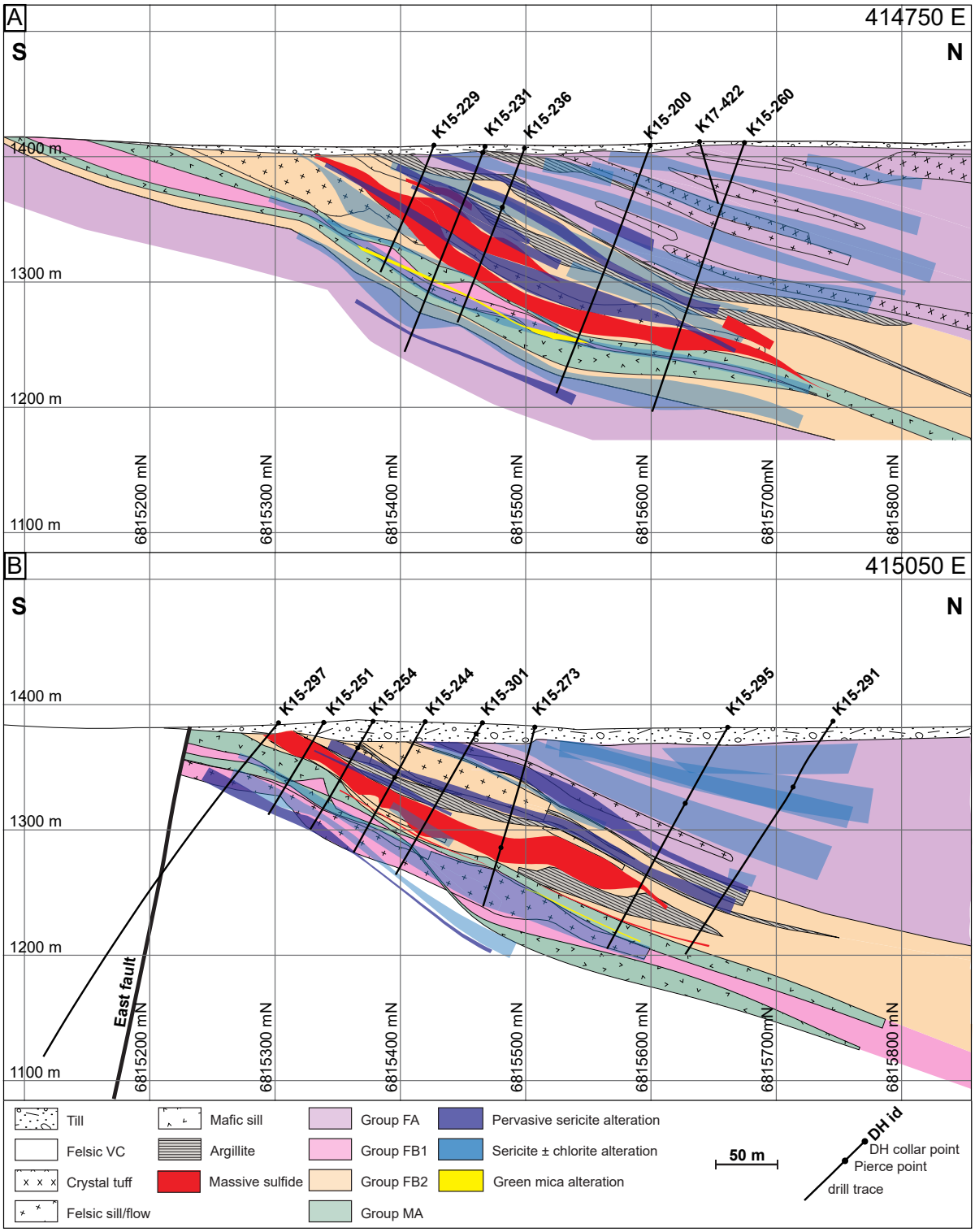

Fig. 3. Cross sections through the ABM zone of the ABM deposit, cross sections are running N-S, looking west. Positions of section lines shown in Figure 2. Abbreviations: DH = drill hole, FA = felsic A, FB = felsic B, MA = mafic A, VC =volcaniclastic rock.

micaceous material >5 µm observed petrographically, and where its composition has been determined using electron microprobe analysis (EMPA), the correct mineral name will be used (muscovite, illite, illite/smectite).

Major and trace element lithogeochemistry methods

Three separate lithogeochemical analytical packages (ME-MS81d, IMC-100, IML-101) were used to analyze the data, to cover all elements necessary to study hydrothermal al-

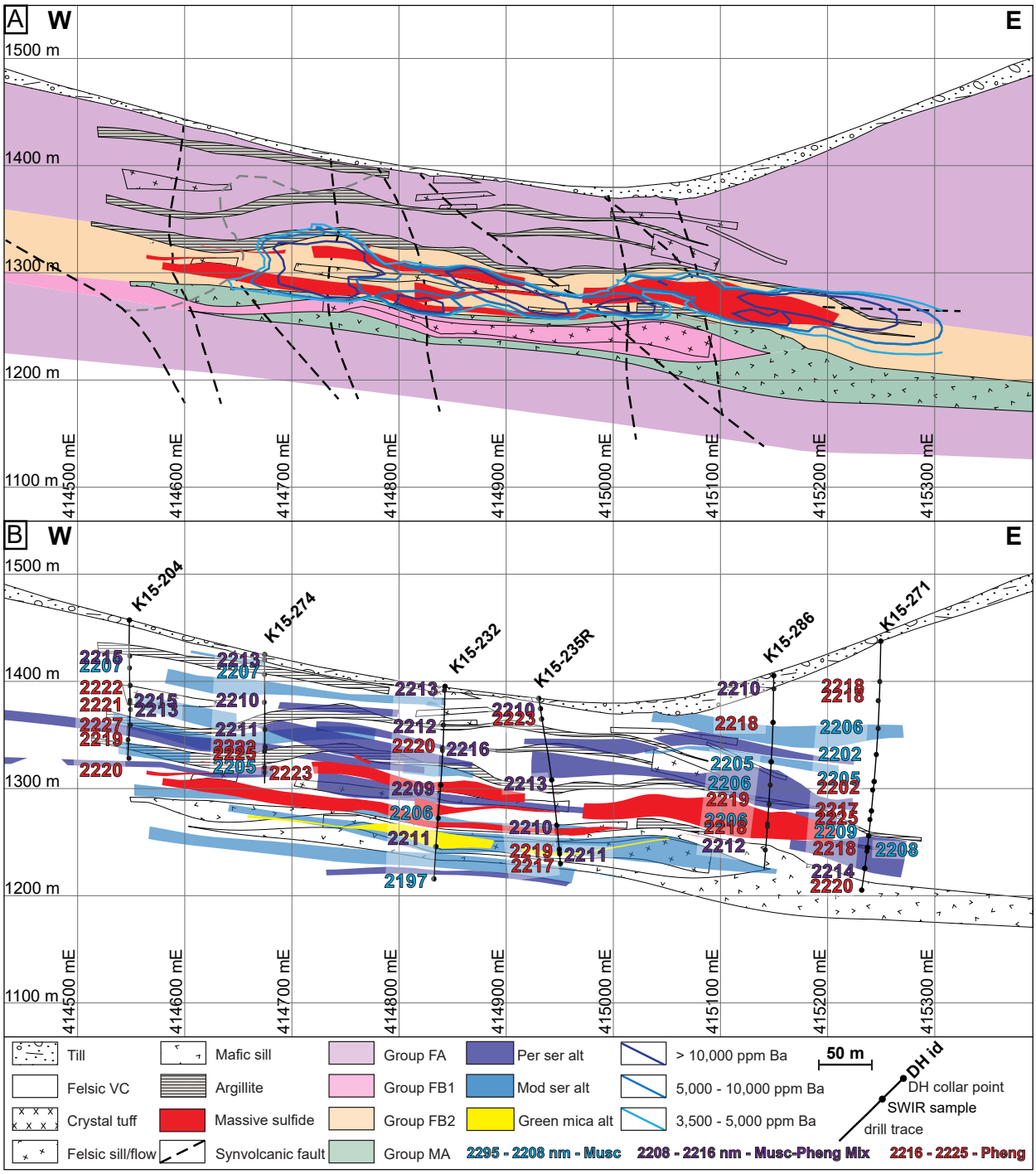

Fig. 4. Long section through the ABM zone of the ABM deposit running W-E, looking north. Drill holes are not clipped to section, entire extent of drill hole displayed. Section line position shown in Figure 2. A) Lithostratigraphy and Ba content contours shown. B) Mineralization, modeled alteration zones, and 2,200-nm feature short-wave infrared (SWIR) values displayed. Abbreviations: DH = drill hole, FA = felsic A, FB = felsic B, MA = mafic A, mod ser alt = moderate sericite alteration, musc = muscovite, per ser alt = pervasive sericite alteration, pheng = phengite, VC =volcaniclastic rock.

teration. The full data set is available in Appendix 1. Sample preparation and analysis methods, together with the quality assurance and quality control procedures for the major and trace element data for the first two packages given below, were presented in detail in Denisová and Piercey (2022). Sample preparation and measurement of major and trace element data (including immobile elements, e.g., Zr, Th, REEs; ME-MS81d) were performed at ALS Laboratories, North Vancouver, British Columbia. Sample powders were fused with a lithium metaborate flux; the fused beads were then cooled and digested using 4% HNO_3-2% HCl mixture. Analyses of the sample solutions were conducted using inductively

coupled plasma-atomic emission spectrometry (ICP-AES) for major elements and inductively coupled plasma-mass spectrometry (ICP-MS) for immobile trace elements (e.g., Zr, Hf, Nb, Ta, Th, U, REEs). The sample suite was also analyzed at Ontario Geoscience Laboratories in Sudbury, Ontario (OGL) to obtain transition metals, base metals, and semimetals (e.g., Li, Be, Co, Cu, Zn, Mo, Cd, In, Sb, W, Bi, Pb, Sc, Ta) using a closed-beaker HF-HCl-$HClO_4$ digest followed by an analytical finish using a Perkin-Elmer Elan 9000 inductively coupled plasma-mass spectrometer (ICP-MS, method IMC-100). Additionally, the same sample suite was further analyzed using an aqua regia extraction method at the same lab, also with an analytical finish using a Perkin-Elmer Elan 9000 ICP-MS, to obtain minor and trace elements (e.g., Sb, As, Bi, Cd, Co, Cu, Au, In, Ir, Pb, Hg, Mo, Ni, Pd, Pt, Se, Ag, Te, Tl, Sn, Zn; method IML-101). The methodologies from OGL outlined above are detailed in Burnham and Schweyer (2004) and Burnham (2008).

Over the course of this study, eight in-house reference material samples (SLV-MC basalt and WP-1 dacite) and several lab duplicates were analyzed at OGL to monitor analytical accuracy and reproducibility (App, 2). For the IMC-100 method, trace element concentrations overall gave relative standard deviation (RSD) values <10%, except for Tl (<19 %) in both WP-1 and SLV-MC. The results for both reference materials overlap with published values (WP-1; Piercey et al., 2001b; Manor and Piercey, 2019) and unpublished in-house data for both SLV-MC and WP-1 with reproducibility better than 10% for most trace elements, with exception of Cd and Cu in the WP-1 dacite that show the percent relative differences <17%. The blind and lab-chosen duplicates show relatively higher RSD values but are generally <15% for most major and trace elements. For the IML-101 method, trace element concentrations overall gave RSD values <10%, except for Mo and In (<16%), and Tl (<30%) in WP-1 and Cd (<11%) in SLV-MC. The results for both reference materials overlap with unpublished in-house data for both SLV-MC and WP-1 with reproducibility better than 10% for most trace elements, with exception of Tl (<51%) in the WP-1 dacite and Cd (<17%) in the SLV-MC basalt. The blind and lab-chosen duplicates show relatively higher RSD values but are generally <15% for most major and trace elements. The aqua regia digestion is devised to leach only elements bound loosely in less resistant mineral phases like sulfides, Fe and Mn oxides, sulfates, carbonates, and some silicates, whereas the HF-HCl-$HClO_4$ digestion dissolves all but the most resistant minerals like zircons and chromites. The two different digestion methods were chosen to better understand the relative distribution of elements like Cd, Cu, In, Mo, Pb, Sb, Tl, and Zn and elucidate whether these elements are bound in the more resistant silicates, or whether they occur in sulfides or adsorbed onto clays and would therefore be released by the less aggressive aqua regia digest.

Electron probe microanalysis

The composition of white mica, chlorite, and carbonate in nine polished thin sections was analyzed at Memorial University using the JEOL JXA-8230 SuperProbe electron probe microanalyzer (EPMA) equipped with five wavelength-dispersive spectrometers (WDS), a Thermo energy-dispersive spectrometer (EDS), and a W electron gun. Natural and synthetic standards were used for calibration of the instrument, where standards and X-ray lines were used on five respective crystals (spectrometers); average detection limits for each element are in parentheses: (1) LDE1: apatite (F*Ka*; 275 ppm); (2) LIFL: almandine (Fe*Ka*; 70 ppm), vanadium (V*Ka*; 39), rutile (Ti*Ka*; 54 ppm), $BaSO_4$ (Ba*La*; 155 ppm); (3) PETL: tugtupite (Cl*Ka*; 26 ppm), orthoclase (K*Ka*; 30 ppm), diopside (Ca*Ka*; 39 ppm), celestite (Sr*La*; 106 ppm); (4) TAP: albite (Na*Ka*; 68 ppm), albite (Al*Ka*; 38 ppm), diopside (Si*Ka*; 79 ppm), diopside (Mg*Ka*; 72 ppm); (5) LIFH: chromium oxide (Cr*Ka*; 40 ppm), rhodonite (Mn*Ka*; 52 ppm), willemite (Zn*Ka*; 92 ppm). Counting times for calibration are 10 s on peaks and 5 s on background. Analyses on unknowns were performed using the same crystals as the calibration. White mica was analyzed for 14 elements (Si, Al, Sr, Ba, Zn, Fe, Mg, Mn, Ca, Na, K, Ti, F, and Cl), chlorite grains were analysed for 16 elements (Si, Al, Fe, Ba, Sr, Cr, V, Zn, Mg, Mn, Ca, Na, K, Ti, F, and Cl), and carbonates were analyzed for 7 elements (Fe, Ba, Ca, Sr, Mg, Mn, and Zn). Silicates were analyzed using an accelerating voltage of 15 kV, a 20-nA beam current, focused to 3 to 5 µm, with elemental counting times between 5 and 60 s. Carbonates were analyzed using an accelerating voltage of 20 kV, a 5-nA beam current, defocused to 8 to 15 µm, with elemental counting times between 5 and 30 s. Internal standards were measured periodically and showed no irregularities. Samples with totals falling outside of typical range of mineral composition minus H_2O were rejected; in the case of micas this was for totals <85%, in the case of chlorites <82%, and in the case of carbonates, where the back-calculated CO_2 values were >60%. Mineral formulas of white mica were calculated based on 11 O; chlorite formulas were calculated based on 14 O.

Short-wave infrared spectroscopy

Hyperspectral measurements of the samples from the original sample suite, together with additional samples, 576 analyses in total, were collected at Memorial University using the Terraspec™ Infrared Spectrometer with a Hi-Brite Muglight. To monitor the accuracy and precision of the acquired data, an internal reference sample (pyrophyllite) was measured after each white reference optimization, which occurred every 20 samples or every 20 minutes during the run of the instrument. The monitoring confirmed that the instrument yielded absorption hulls that were consistently within 3 nm of accepted values for the internal standard. Data was processed using The Spectral Geologist 7.1 software. Hyperspectral scalars were calculated for the 2,200-nm (2,185–2,225 nm) and 2,250-nm (2,245–2,265 nm) absorption wavelengths features using a fourth-order polynomial fitting curve, with hull correction and background noise filters applied to the spectra. The diagnostic absorption feature for white mica occurs between 2,180 and 2,225 nm and is caused by the variation in composition due to the Tschermak substitution ($Al^{VI} + Al^{IV} \leftrightarrow (Fe, Mg, Mn)^{VI} + Si^{IV}$), and by the interlayer cation substitution between K and Na (Velde, 1978; Herrmann et al., 2001; Yang et al., 2011). Values of the 2,200-nm feature between 2,180 and 2,195 nm are attributed to Na-bearing muscovite, between 2,200 and 2,208 nm are considered to be muscovite; wavelengths of 2,216 to 2,228 nm have a phengite composition, and values in between 2,208 and 2,216 nm are considered to be mixtures of two or

more mica phases, or to have an intermediate composition (Herrmann et al., 2001; Jones et al., 2005; Yang et al., 2011). For chlorite, the 2,250-nm absorption feature between 2,235 and 2,255 nm is controlled by the Fe content, with higher absorption values indicating higher Fe content of the chlorite. (Herrmann et al., 2001; Cloutier et al., 2021). Most of the samples from the ABM deposit are mixed samples; therefore, the depth of the above-described absorption features to determine relative mineral abundance is of limited use, but in general, the deeper the absorption feature, the higher the relative abundance of the mineral (Cloutier and Piercey, 2020).

Observations and Results

Hydrothermal alteration at the ABM deposit

The observations presented in this section are based on drill core and petrographic observations. Alteration in the ABM deposit occurs both in the hanging wall and footwall of the massive sulfide lenses (Figs. 3, 4) and consists of five main assemblages: pervasive sericite, pervasive chlorite, moderate to weak sericite ± chlorite, chlorite-carbonate-actinolite, and Fe carbonate. The alteration assemblages and their intensities do not differ significantly between the hanging wall and footwall, and no alteration assemblage is bound to a particular stratigraphic unit or position, except for those restricted to a specific rock type (e.g., chlorite-carbonate-actinolite assemblage in mafic sills in Sequence 2). Alteration zones are generally stratabound (Fig. 3, 4), but in rare cases, they cross lithological boundaries, and there are mostly gradual transitions between the different assemblages. Locally, sharp contacts occur between pervasive chlorite alteration and paragenetically earlier alteration assemblages. The pervasive sericite and chlorite alteration assemblages occur in proximity to the mineralization, commonly within 100 m of mineralization into the hanging wall or footwall. Less pervasive alteration assemblages extend up to 1,400 m west along strike and 500 m downdip, and typically these assemblages are weak sericite ± chlorite assemblages; however, even in these weakly altered areas, there are some localized zones of pervasive alteration implying that there are other possible mineralized zones in the area (Fig. 2). The following sections will describe the distribution, extent, mineralogy, and textures present of each major alteration assemblage, and their relationship to the mineralization.

Pervasive sericite alteration assemblage: Zones of pervasive sericite alteration occur in all felsic lithologies in the ABM deposit in both the hanging wall and footwall to the mineralization (Figs. 3, 4). The alteration zones are stratabound, up to ~25 m thick, and extend along strike and downdip. Contacts with surrounding zones of moderate sericite ± chlorite alteration are gradual. Locally, individual lapilli, quartz, or feldspar crystals are preserved (Fig. 5A). The assemblage is dominated by white mica, which makes up between 15 and 45 modal %. Tabular white mica grains have roughly similar size (100–200 μm) and replace the matrix, and their alignment defines the fabric, which is oriented subparallel to the lapilli or other preserved features within the felsic rocks (Fig. 5B-C). White mica commonly overprints remnant primary minerals including K-feldspar or plagioclase, and locally minor early alteration minerals like dolomite. Carbonate, chlorite, and biotite are minor (commonly ≤5 modal %) and paragenetically contemporaneous with or later than the white mica. Minor (<1% volume) disseminated fine- to medium-grained sulfide grains (pyrite and pyrrhotite) are present and, locally, discontinuous sulfide stringers or rare diffuse bands of sulfides occur in this assemblage. In proximity to the massive sulfide mineralization, some pervasively sericite-altered intervals are locally fissile and extensively fractured, likely due to the abundance of white mica (Fig. 5D). Locally, these fractured intervals also contain irregular, milky white quartz veins with minor associated carbonate, sulfide, and/or rare tourmaline or biotite. These veins are paragenetically late (postdeformation) but formed before the extensive fracturing.

Pervasive chlorite alteration assemblage: Zones of pervasive chlorite alteration are stratabound, on average ~2 m thick, and affect both felsic and mafic lithofacies. This alteration assemblage occurs commonly on the hanging wall or footwall contacts of massive sulfide lenses and/or within the lenses themselves, and also on the contacts of the mafic subvolcanic sills in Sequence 2. Contacts with mineralization are gradual, whereas with pervasive sericite and moderate sericite ± chlorite alteration zones they are sharp (Fig. 5E). The rocks are dark green due to pervasive replacement by very fine grained to fine-grained green chlorite, and primary igneous textures are rarely preserved. The assemblage contains two subtypes: one that is barren of mineralization (Fig. 5F), and a second spatially associated with sulfide and magnetite mineralization (Fig. 5G). The two subtypes most commonly occur separately but locally gradually transition into each other. The first, barren subtype of the assemblage contains between 15 and 60 modal % chlorite (Fig. 5F, H); bands of bladed chlorite define the fabric and overprint the primary minerals and minor biotite replacing chlorite (Fig. 5H). In the second mineralization-

Fig. 5. Alteration assemblages present at the ABM deposit. A) Pervasive sericite alteration in lapilli tuff; K15-290 m, 59 m downhole. B) Fabric preserved in pervasively sericite altered tuff; K15-320, 200 m downhole. C) Pervasive sericite alteration in thin section, white mica bands, later coarser carbonate alteration; B370151; K15-295, 188.3 m downhole. D) Fissile pervasively sericite altered drill core; K15-287, 31 m downhole. E) Sharp contact of pervasive chlorite alteration over pervasive sericite alteration; K17-422, 165 m down hole. F) Barren pervasive chlorite alteration; K15-287, 118 m down hole. G) Mineralized pervasive chlorite alteration; K15-235R, 140 m down hole. H) Barren pervasive chlorite alteration in thin section; Q721071; K15-287, 118.45 m downhole. I) Mineralized pervasive chlorite alteration in thin section; Q930216; K15-232; 142.1 m downhole. J) Sulfide stringers in pervasive chlorite alteration; K14-281, 197 m downhole. K) Moderate sericite ± chlorite alteration in crystal-lapilli tuff; K15-271, 40 m downhole. L) Sericite ± chlorite alteration in matrix; K15-260, 204 m downhole. M) Bands of illite in thin section of sericite ± chlorite alteration; B370159; K15-301, 91.3 m downhole. N) K-feldspar in K-feldspar-quartz clot replaced by mica; Q930295; K15-315, 151.65 m downhole. O) Disseminated pyrite in moderate sericite ± chlorite altered tuff; K15-320, 261 m downhole. P) Green mica alteration with bands of sphalerite and carbonate; K15-232, 175 m downhole. (Q) Fe carbonate alteration in sericite ± chlorite tuff; K15-271, 60 m downhole. R) Euhedral albite overprinted by chlorite and chalcopyrite-pyrrhotite-sphalerite; K7-422, 160.9 m downhole. Abbreviations: Carb = carbonate, K-fsp = K-feldspar, Mica = white mica, Qtz = quartz.

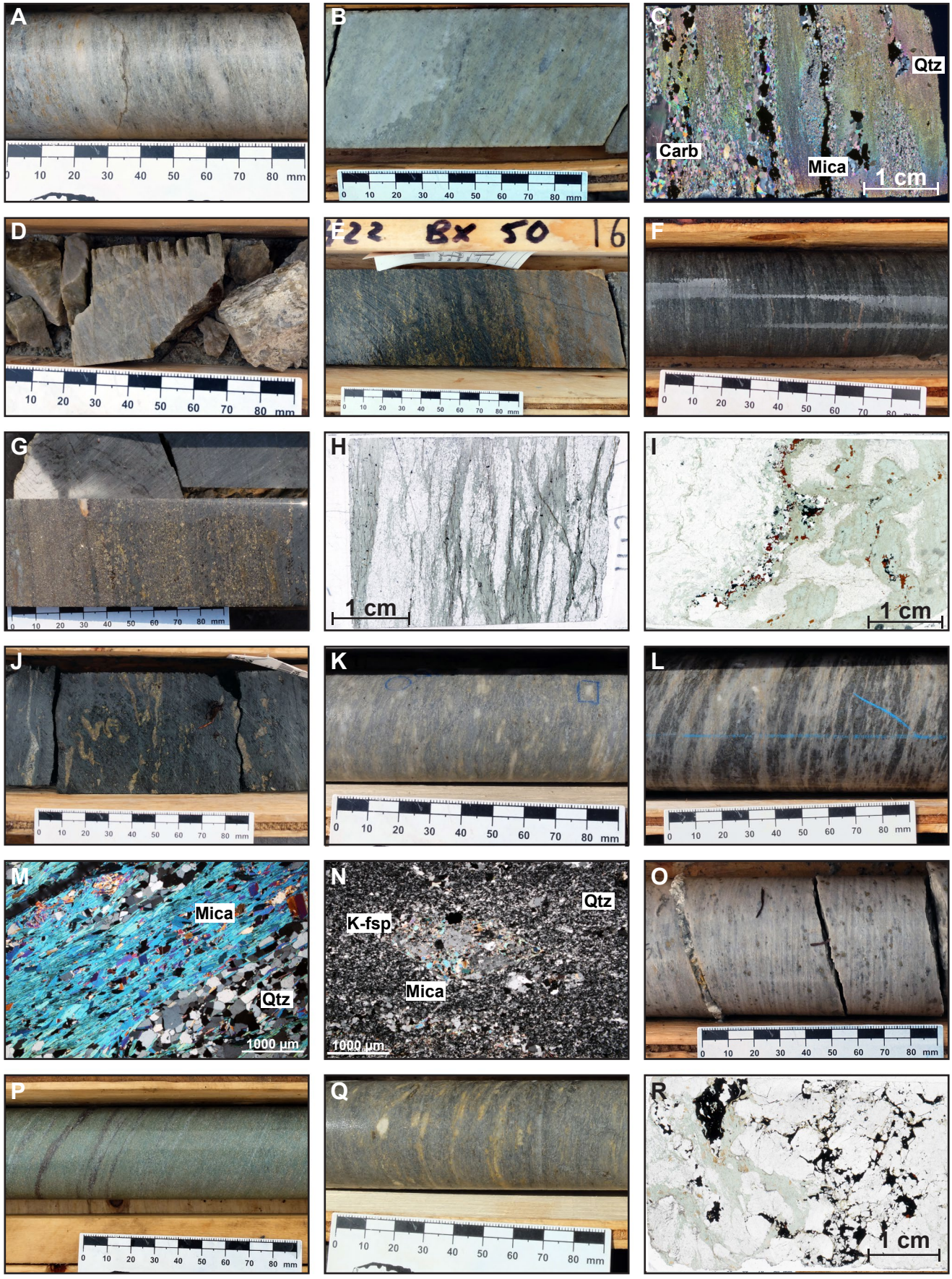

associated subtype, chlorite is the dominant phase (locally with black chlorite grains up to 5 cm in size) but composes only up to 30 modal %; white mica, biotite, and carbonate occur at higher proportions than in the barren subtype (Fig. 5I). Both white mica and chlorite define the fabric in the mineralized subtype of this alteration assemblage. Sulfides are one of the paragenetically latest phases in the mineralized subtype, occurring as stringers, irregular patches, or disseminated grains. Chalcopyrite-pyrrhotite-pyrite veinlets and stringers are the most common sulfides (Fig. 5J) with lesser magnetite, sphalerite, galena, and sulfosalts. The proportion of sulfides increases with proximity to the massive sulfide lenses.

Moderate to weak sericite ± chlorite alteration assemblage: The moderate to weak sericite ± chlorite alteration assemblage is the most widespread assemblage in the ABM deposit and consists of white mica and lesser chlorite, with minor carbonate, sulfides, and biotite. This assemblage is ubiquitous across the volcanosedimentary package and occurs up to the conformable contact with the Wind Lake formation. It occurs in felsic volcaniclastic and volcanic rocks and commonly varies from moderate to weak in intensity, with gradual transitions in between. The rocks are greenish in color due to the abundance of yellow-green sericite. Primary textures are preserved in the host rocks, and the alteration affects the groundmass/matrix predominantly; the orientation of the alteration mineral grains roughly aligns with the fabric defined by the remnant primary igneous features (Fig. 5K). Locally, the lapilli in volcaniclastic rocks are affected by a different alteration assemblage than the matrix and contain chlorite, biotite, carbonate, and/or sulfides, typically pyrite or pyrrhotite (Fig. 5L). In thin section, white mica comprises between 5 and 30 modal %, and bladed white mica grains occur most commonly in bands that define the fabric (Fig. 5M); relict feldspar grains are partly to fully replaced by fine white mica (Fig. 5N). Chlorite is less common than white mica in this assemblage, commonly <10 modal % where it occurs, and in most cases overprints the mica-defined fabric. Minor biotite locally overprints or replaces chlorite. Fine-grained disseminated sulfides (dominantly pyrite) and carbonate are commonly the paragenetically latest phases (Fig. 5O). Where the alteration assemblage affects coherent felsic rocks, minor carbonate-sulfide veinlets with random orientations occur. In the central part of the ABM zone within Sequence 2 (Fig. 4), pale green intervals contain green mica intergrown with sericite. The green mica-sericite assemblage is limited to the contacts of the mafic sills with other rocks and to the contacts of the felsic sill that is enclosed in between the two mafic sills (Fig. 4). Green mica is very fine grained and green mica-altered intervals gradually transition into sericite-rich intervals. Carbonate bands up to 30 cm thick occur in the green mica-rich intervals and are commonly associated with lesser red sphalerite and minor galena and pyrite/pyrrhotite (Fig. 5P). The green mica-altered intervals of felsic volcanic rocks have elevated Cr content (~600 ppm Cr in one available sample) compared to felsic rocks of the Kudz Ze Kayah formation affected by different alteration assemblages (<30 ppm Cr); mafic sills with MA signatures (see "Key immobile elements" section) contain high Cr values (>290 ppm Cr; Denisová and Piercey, 2022).

Fe-carbonate alteration: Carbonate with significant Fe content, in addition to Ca and Mg, typically occurs as the paragenetically latest mineral phase in drill core. It occurs as dispersed euhedral grains or as coatings on grains, lapilli, or other heterogeneities and has an orange color in older (>2 years) drill core (Fig. 5Q). It occurs across the stratigraphy and affects all lithological units in the upper Kudz Ze Kayah formation and the argillites and mafic tuffs in the lower Wind Lake formation.

Chlorite-carbonate-actinolite assemblage: The chlorite-carbonate-actinolite assemblage occurs only in the mafic sills in Sequence 2; no unaltered or less altered mafic sills exist in the ABM deposit footprint. Contacts of the mafic sills are commonly finer grained and more intensely altered with carbonate and, locally, biotite compared to the inner portions of the sills, which have a dark green, fine-grained groundmass with aligned darker biotite-chlorite–rich patches, assumed to be replaced primary mafic mineral phenocrysts (Fig. 6A-B). The assemblage replaces most of the primary igneous minerals, yet primary igneous textures are partially preserved and overprinted by the alteration minerals (Fig. 6A). The assemblage consists of abundant chlorite (10–35 modal %), carbonate (5–20 modal %), biotite (5–20 modal %), actinolite (20–25 modal % if present), and paragenetically late epidote (5–15 modal %). Carbonate, chlorite, and minor white mica replace the groundmass (Fig. 6C), and white mica and carbonate commonly replace K-feldspar and plagioclase, respectively. Corroded euhedral to subhedral equant actinolite grains are commonly replaced by chlorite and/or biotite (Fig. 6D), although late amphibole needles are observed locally. Barium-rich K-feldspar is found along biotite cleavage planes (Fig. 6E). The paragenetically youngest mineral phase is commonly euhedral, fine-grained epidote (Fig. 6F).

Paragenesis: Crosscutting relationships determined from drill core and thin sections are used to establish the paragenesis of the different alteration assemblages in the ABM deposit (Fig. 7). The moderate sericite ± chlorite assemblage is interpreted to be the paragenetically oldest one preserved in the ABM deposit. It has the widest extent within the upper Kudz Ze Kayah formation (Fig. 2B) and is overprinted by both pervasive assemblages. The contacts between moderate sericite ± chlorite and pervasive sericite alteration zones are commonly gradual. Pervasive chlorite alteration overprints the pervasive sericite assemblage and commonly has sharp contacts (Fig. 5F). Sulfide mineralization crosscuts both pervasive assemblages. Contacts with mineralization are sharp (Fig. 8); rarely, they are gradational over 10 to 20 cm. The paragenetically youngest observed phase is fine-grained, diffuse Fe-rich carbonate or calcite, with minor euhedral Fe carbonate and calcite grains overprinting all other assemblages (Fig. 5Q-R).

Key immobile elements characteristics of host rocks

Denisová and Piercey (2022) described the immobile element systematics of the volcanic rocks of the upper Kudz Ze Kayah formation. Immobile behavior of HFSE (high field strength elements)-REE (rare earth elements)-Al_2O_3-TiO_2 was assessed and confirmed using methods defined by MacLean (1988) and MacLean and Barrett (1993). Felsic rocks of the upper Kudz Ze Kayah formation plot on a single linear array in the Zr-TiO_2 space (Fig. 9A), therefore immobile element ratios have been employed to further differentiate between the rock types and chemostratigraphic units. In the Al_2O_3/

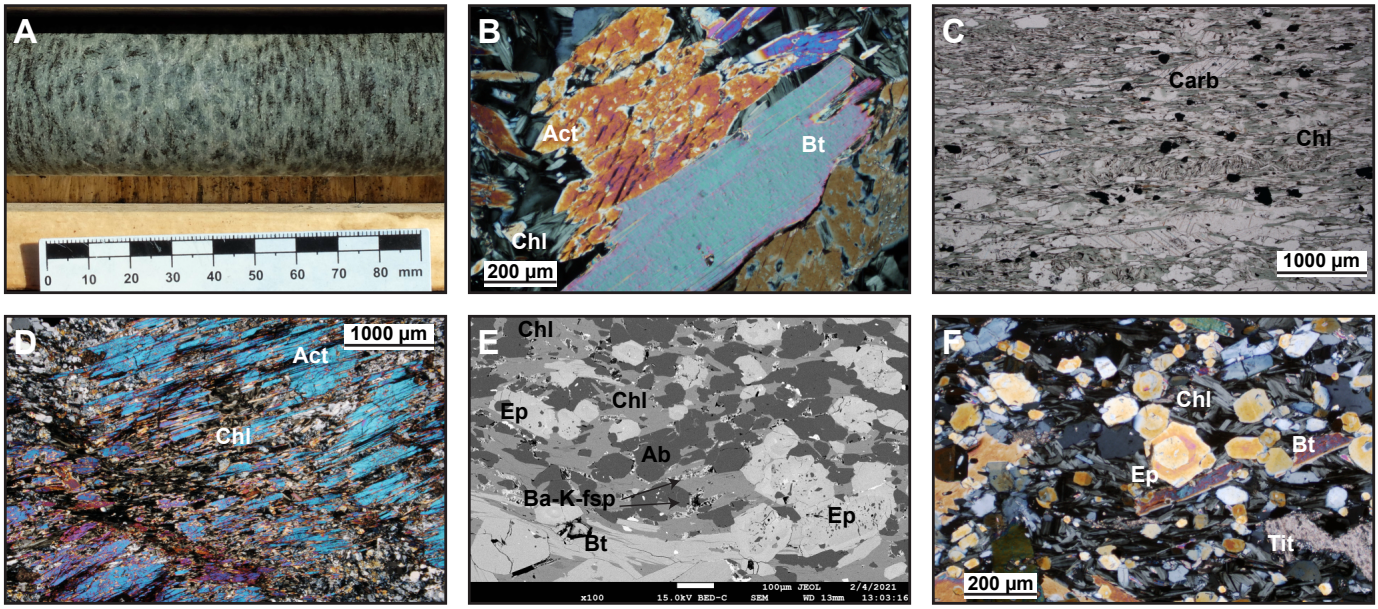

Fig. 6. Alteration assemblages in mafic sills with Mafic A (MA) signatures. A) Coarse-grained interior of mafic sill in Sequence 2 with amphibole-biotite clots; K15-265, 245 m downhole. B) Biotite overgrowing amphibole, core of mafic sill; AA00348399; K15-290, 117.4 m downhole. C) Barren chlorite alteration in thin section, margin of mafic sill; AA00348398; K15- 290, 90.8 m downhole. D) Chlorite replacing amphibole, core of mafic sill; K15-290, 117.4 m downhole. E) Ba-rich K-feldspar along fractures and grain boundaries in chlorite, late zoned epidote grains overgrowing; Q930290; K15-315, 121 m downhole. F) Late zoned epidote grains overgrowing biotite and chlorite; Q930291, K15-315, 122 m downhole. Abbreviations: Ab = albite, Act = actinolite, Ba-K-fsp = Ba-K-feldspar, Bt = biotite, Carb = carbonate, Chl = chlorite, Ep = epidote, Tit = titanite.

TiO_2-Zr/Al_2O_3 space, two distinct groupings of felsic volcanic rocks exist (Fig. 9B). Group Felsic A (FA) has high Zr concentrations (722 ± 118 ppm, n = 33) and generally higher contents of HFSEs relative to the group Felsic B (FB). The FB group is further divided into subgroups FB1 and FB2, based on differences between immobile elements and their ratios, with group FB1 having a higher average Zr value (419 ± 101 ppm, n = 16) than subgroup FB2 (267 ± 91 ppm, n = 26). Felsic rocks belonging to the FB group occur in Sequence 2 and host the massive sulfide mineralization. Sequences 1 and 3 comprise felsic volcanic rocks of group FA. Mafic rocks of the upper Kudz Ze Kayah formation fall into two distinct groups based on their immobile element compositions (Fig. 9A, B): group Mafic A (MA) comprises mafic sills in Sequence 2, whereas group Mafic B (MB) represents younger mafic sills present in Sequence 3.

Major and mobile trace elements

Using major oxides to trace hydrothermal alteration is a simple but effective technique utilized in VMS environments to track alteration processes such as feldspar destruction and subsequent white mica (Na_2O, CaO, K_2O), chlorite, and pyrite formation (MgO, Fe_2O_3; Spitz and Darling, 1978; Riverin and Hodgson, 1980; Date et al., 1983; Large et al., 2001c; Mathieu, 2018).

In the alteration box plot (Fig. 9C; Large et al., 2001b), samples identified by other methods as least altered (Fig. 9D; the Na_2O-Na_2O/Al_2O_3 diagram; Ruks et al., 2006) plot within the least altered rhyolite and dacite fields. Most of the felsic samples follow the sericite alteration path, with data plotting on a trend from the least-altered fields toward the illite (sericite) node (trend 2 in Figure 9C). Rocks with FB signatures from Sequence 2 (proximal to the mineralization) show a more significant shift toward sericite than the FA rocks that are more distal from the massive sulfide mineralization. Samples that follow the chlorite-pyrite and sericite-chlorite-pyrite trends are strongly to pervasively altered by white mica and/or chlorite (trend 1 in Figure 9C). A minor subset of the felsic samples follows a diagenetic trend toward the albite node, indicating that they underwent diagenetic alteration that is locally preserved (trend 3 in Figure 9C). Observed textures show euhedral albite grains locally overprinted by chlorite and mineralization (Fig. 5R) or minor white mica. Feldspar destruction and common sericite alteration are also easily distinguishable in molar ratio plots of K_2O and Na_2O (Davies and Whitehead, 2006), where FB felsic rocks show strong feldspar destruction and sericite alteration (Fig. 9E). Large ion lithophile elements (LILEs) such as Rb and Sr correlate with the behavior of their geochemical twins, K and Ca, respectively (Fig. 9F-G).

In different types of VMS deposits, mobile metallic and metalloid trace elements (Sb, Tl, Mn) form halos of varying magnitude around the massive sulfide lenses (Large et al., 2001a, c). At the ABM deposit, some of these elements increase proximal to mineralization (Fig. 10). Thallium and Sb, both volatile elements, correlate well and show elevated values in proximity to massive sulfide mineralization (Fig. 9H). Anomalous values of Tl and Sb occur up to 300 m from the massive sulfide lenses in all directions. Arsenic, Bi, Cd, Mo, and Sn values are higher within Sequence 2 rocks compared to other sequences but do not show consistent increases with proximity to mineralization (Fig. 10). Base metals abundant in the mineralization (Zn, Cu, Pb) and Au and Ag follow a similar pattern; they are slightly increased within Sequence 2

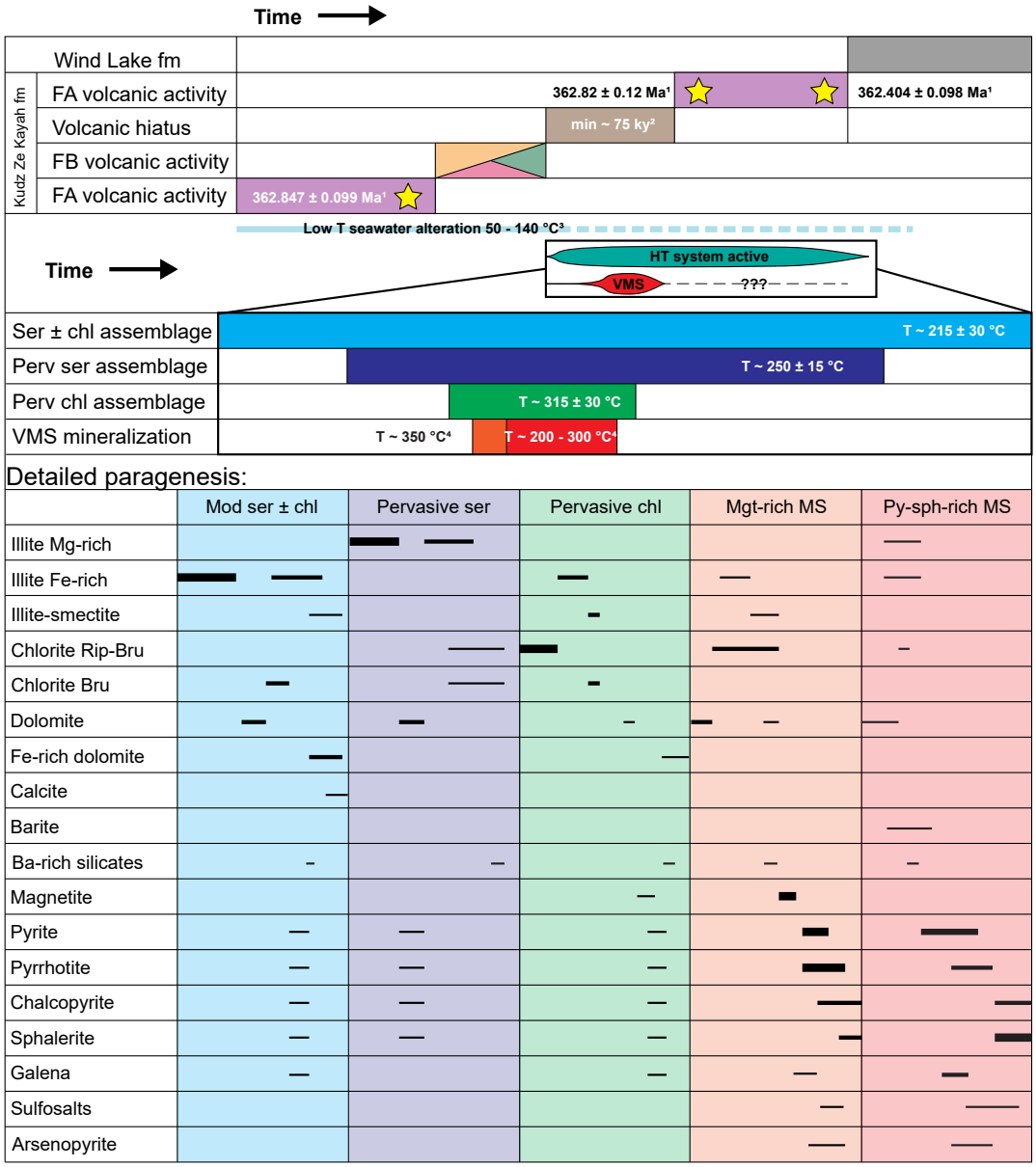

Fig. 7. Paragenesis at the ABM deposit. [1]Manor et al. (2022b); [2]Denisová and Piercey (2022); [3]Gifkins and Allen (2001); [4]Franklin et al. (2005). Colors correspond to previous figures. Abbreviations: bru = brunsvigite, FA = Felsic A, FB = Felsic B, HT = hydrothermal, MS = massive sulfide, perv chl = pervasive chlorite, perv ser = pervasive sericite, rip = ripidolite, VMS = volcanogenic massive sulfide

rocks compared to other sequences (App. 3). Manganese and In display relatively higher values in Sequence 3 rocks compared to Sequence 2 rocks (Fig. 10), although rare anomalous values occur associated with massive sulfide mineralization (Fig. 10).

Mass balance

Mass balance calculations for felsic volcanic rocks were performed using the single precursor method outlined by in MacLean and Barrett (1993) and Barrett et al. (2008). No unaltered samples of mafic volcanic rocks were identified from hand samples or from geochemical data, therefore mass balance calculations were not performed for mafic rocks in the ABM deposit footprint. Samples of the FA and FB felsic geochemical groups plot on separate linear arrays in Al_2O_3/TiO_2-Zr/TiO_2 space (Fig. 9B), which indicates they belong to two distinct homogenous volcanic units (Barrett et al., 2008). Least-altered samples from the felsic geochemical groups (FA, FB1, and FB2; App. 4a) were selected based on low loss on ignition (LOI) values (<2.5%), low base metal values (Zn + Pb + Cu < 500 ppm), relatively high Na_2O content (>2%), and low Spitz-Darling index (Al_2O_3/Na_2O <10; Spitz and Darling, 1978; Ruks et al., 2006). The least-altered values were averaged to establish a precursor composition for each geochemical group, with Al_2O_3 used as the monitor of mass change (Barrett et al., 2008). Least-altered samples were chosen from both the project data set (this study and Denisová and Piercey, 2022) and the BMC lithogeochemical

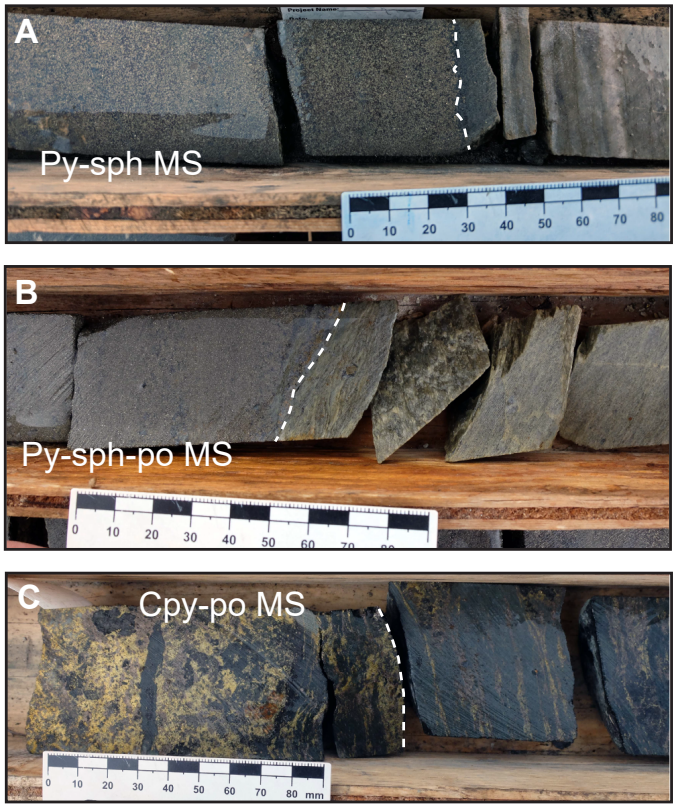

Fig. 8. Examples of mineralization overprinting alteration assemblages. A) Sharp contact between pyrite-sphalerite mineralization and moderate sericite ± chlorite altered tuff; K15-240, 54.5 m downhole. B) Sharp contact between pyrite-sphalerite-pyrrhotite mineralization and pervasively sericite altered tuff; K15-287, 47 m downhole. C) Chalcopyrite-pyrrhotite mineralization overprinting pervasive chlorite alteration; K17-422, 149.5 m downhole. Abbreviations: Cpy = chalcopyrite, MS = massive sulfide mineralization, Po = Pyrrhotite, Py = pyrite, Sph = sphalerite.

database. The company data set contains an incomplete and inconsistent suite of elements compared to new results presented in this study, particularly for minor LILEs (Cs, Rb, Sr) and other trace elements for nonmineralized samples (Sr, Sc, Rb, Tl, Sb, Hg); therefore, mass balance calculations were performed only for the major mobile elements, base metals, and Ba, as these were universal across our new data and the legacy data from the company data set. Calculated values of mass change for felsic samples are presented in Appendix 4b. Most samples show depletions in Na_2O, typical for the destruction of feldspar (Fig. 11A). Commonly, plagioclase destruction can be monitored using both Na_2O and CaO mass changes (MacLean, 1990; Barrett et al., 1993; MacLean and Barrett, 1993), but late carbonate overprints prevent this at the ABM deposit. Samples with $\Delta Na_2O < -1.5$ wt % generally have values of AI (Ishikawa alteration index) >60. Samples with additions of Na_2O (Fig. 11A) coincide with the diagenetic trend in the alteration box plot (Fig. 9C). A minority of FB group samples shows significant additions of K_2O (>3%; Fig. 11B), indicative of pervasive sericite alteration; these samples also show AI >60. Minor samples from groups FB2 and FA show Fe_2O_3 + MgO gains between 7 and 20% and also display mass losses of SiO_2, which is indicative of pervasive chlorite alteration (Fig. 11C). These samples generally have CCPI (chlorite-carbonate-pyrite index) values >65. Samples closest to the mineralization (i.e., FB rocks) show the highest degree of feldspar destruction and locally significant mass gains of Ba (Fig. 11D). Most samples with significant Fe_2O_3 + MgO gains show mass changes of Ba lower than 1,000 ppm. Samples with mass gains of base metals (Zn + Pb + Cu >500 ppm) display losses of Na_2O and locally Fe_2O_3 + MgO gains (Fig. 11E-F). Representative downhole profiles with mass change values are available in Appendix 4c.

Mineral chemistry

Nine samples were selected for the study of the mineral composition of the major alteration minerals (white mica, carbonate, and chlorite). The samples were chosen to be representative of the major alteration types (pervasive sericite - D00005985; pervasive chlorite – D00005986, Q721071, Q721080, Q930216; moderate sericite ± chlorite – D00005981, Q930221, Q931973, Q931984) and to determine the compositional variety of the minerals based on their position in the stratigraphy, alteration intensity, and proximity to massive sulfide mineralization. Full results of the EMPA analyses are given in Appendix 5.

White mica: White mica composition has been calculated based on 11 oxygens with all iron assumed to be Fe^{2+}. The composition of the 152 analyzed grains ranges between $(K_{0.187–0.904}Na_{0.003–0.129}Ba_{0.003–0.047})_{\Sigma 0.21–0.93}$ $(Al_{0.102–2.082}Fe_{0.038–1.938}Mg_{0.053–1.742})_{\Sigma 2.01–3.12}$ $(Si_{2.417–3.563}Al_{0.437–1.582})_{\Sigma 4}$ O_{10} $(OH)_2$. The majority of analyzed white mica grains have compositions typical for illite (Fig. 12B), with the sum of interlayer cations (I) between 0.75 and 0.93 apfu and illite/smectite I between 0.21 and 0.75 apfu. The main interlayer cation is K (0.19–0.90 apfu), with only minor Na (~0.04 apfu) and negligible Ca and Sr. Barium content in the interlayer deficient mica is locally between 0.035 and 0.047 apfu, with an average value of 0.01 apfu. Based on their Fe, Mg, and K content, the interlayer-deficient micas can be divided into three groups (Fig. 12A). The first group (group 1) is illite with a high proportion of Mg compared to Fe (Fe# between 15 and 30%). The second group (group 2) is illite and illite/smectite with a higher proportion of Fe compared to Mg (Fe# ~35–60%). The third group (group 3) is illite/smectite due to its lower cation sum (between 0.2 and 0.5 apfu), while having a similar range of Fe# as group 2 micas. The group 1 illites with higher Mg are present in pervasively sericite-altered felsic rocks proximal to the massive sulfide mineralization, whereas group 2 illites with higher Fe are much more widespread across different alteration types in the sample suite. The group 3 illites/smectites are associated with group 2 illites but appear to postdate them. A subset of the group 2 illites shows slightly elevated Ba values compared to the rest of the sample set, with Ba between 0.031 and 0.029 apfu with rare values up to 0.047 apfu. The occurrence of the Ba-enriched illites is limited to the samples from Sequence 2 in the immediate proximity of mineralization.

Illite geothermometry: Temperatures were calculated for 152 of the analyzed illite and illite/smectite grains using the equation proposed by Battaglia (2004). This method is based on calibrated empirical data from several geothermal fields and quantifies the relationship between illite composition (K, Fe, Mg) and temperature (Cathelineau, 1988; Battaglia,

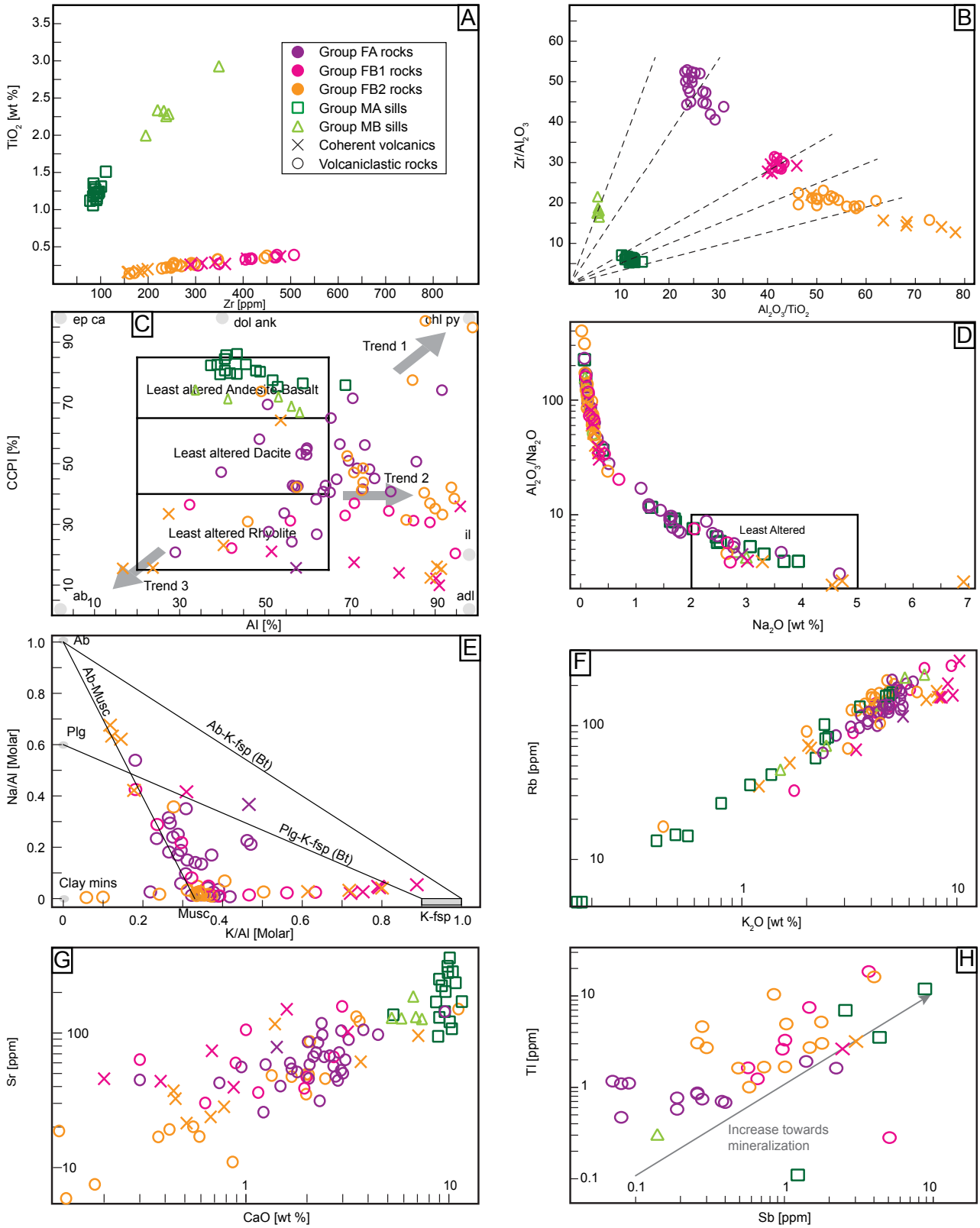

Fig. 9. Major and trace element plots. A) Plot of Zr vs. TiO_2. B) Plot of Al_2O_3/TiO_2 vs. Zr/Al_2O_3. C) Alteration box plot after Large et al. (2001b). D) Na_2O vs. Al_2O_3/Na_2O (Spitz-Darling index) showing least altered rocks after Ruks et al. (2006). E) K/Al vs. Na/Al molar ratio plot of mobile/immobile element after Davies and Whitehead (2006). F) Plot of K_2O vs. Rb. G) Plot of CaO vs. Sr. H) Plot of Sb vs. Tl after Large et al. (2001a). Abbreviations: ab = albite, adl = adularia, ank = ankerite, bt = biotite, ca = calcite, chl = chlorite, dol = dolomite, ep = epidote, FA = Felsic A, FB = Felsic B, il = illite, K-fsp = K-feldspar, MA = Mafic A, MB = Mafic B, mins = minerals, musc = muscovite, plg = plagioclase, py = pyrite

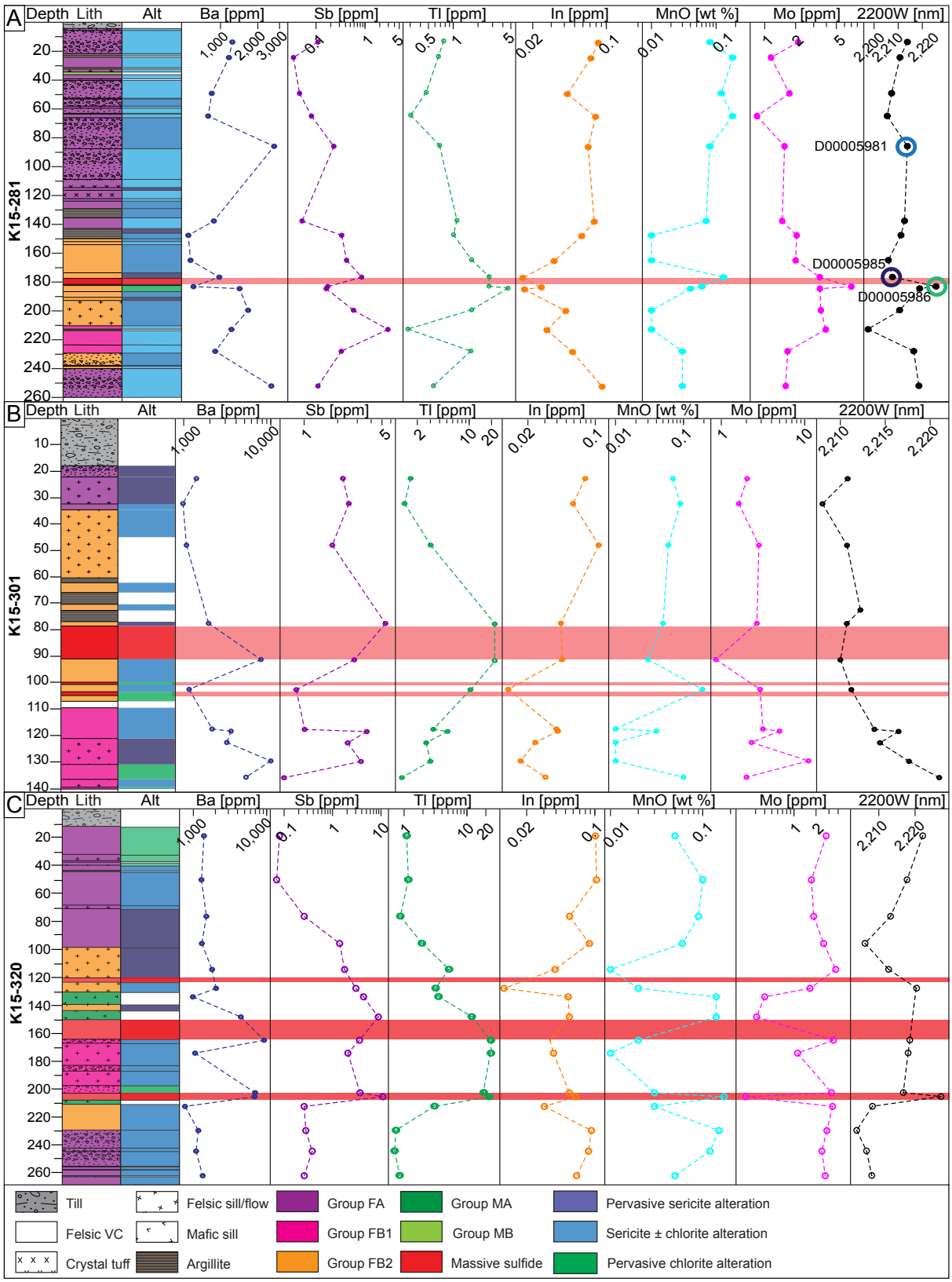

Fig. 10. Downhole profiles of drill holes in the ABM deposit. A) Drill hole K15-281, in the western part of the ABM Zone, position of the drill hole is highlighted in the map in Figure 2A. Highlighted samples part of the electron microprobe analysis (EMPA) data set. B) Drill hole K15-301 in the east part of the ABM Zone, 415050 mE cross section. C) Drill hole K15-320, in the Krakatoa Zone, position of the drill hole is highlighted in the map in Figure 2A. Abbreviations: Alt = alteration, FA = Felsic A, FB = Felsic B, Lith = lithology, MA = Mafic A, MB = Mafic B, VC = volcaniclastic rock.

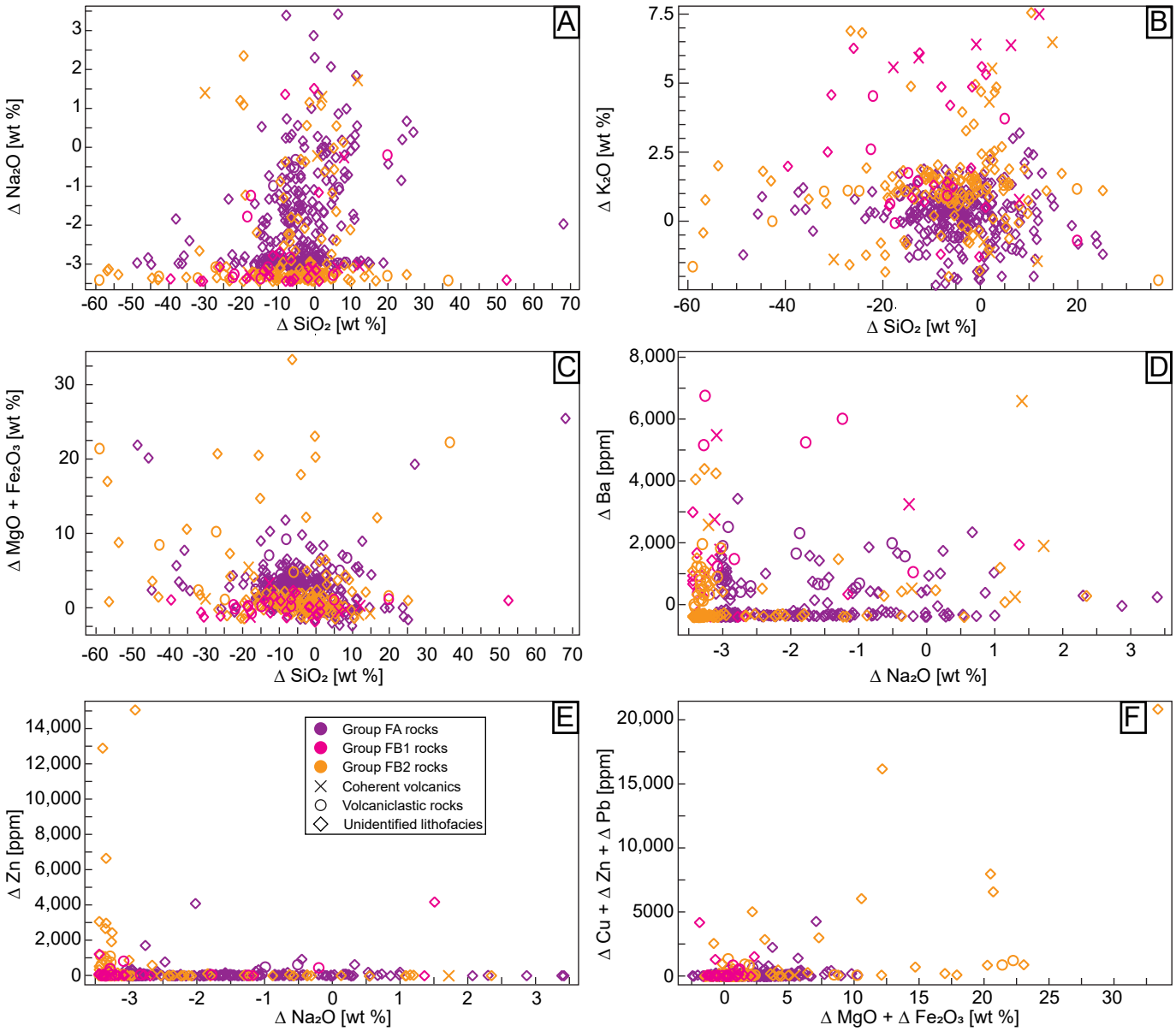

Fig. 11. Mass balance plots of selected elements. A) ΔSiO_2 vs. ΔNa_2O. B) ΔSiO_2 vs. ΔK_2O. C) ΔSiO_2 vs. ($\Delta MgO + \Delta Fe_2O_3$). D) ΔNa_2O vs. ΔBa. E) ΔNa_2O vs. ΔZn. F) ($\Delta MgO + \Delta Fe_2O_3$) vs. ($\Delta Cu + \Delta Zn + \Delta Pb$). FA = Felsic A, FB = Felsic B.

2004). Results from analyzed illite and illite/smectite grains at ABM adhere to the trends described by Battaglia (2004): the calculated temperature rises with higher K content (App. 5). The highest temperatures 249.3° ± 14.9°C are found in the illites with low Fe# (group 1) that occur in the pervasively sericite-altered zone (D00005985). Illite grains with higher Fe# (group 2) from samples from moderate sericite ± chlorite alteration zones have lower temperatures: 219.5° ± 10.2°C (sample D0005981), 223.2° ± 31.8°C (sample Q930221), 204.6° ± 10.8°C (sample Q931973), and 217.8° ±17.5°C (sample Q931984). In a sample from a pervasively chlorite altered zone (sample D00005986), the illite with high Fe# (group 2) has a temperature of 215.3° ± 4.3°C.

Carbonate: Most of the analyzed carbonates have compositions between dolomite ($(Ca,Mg)CO_3$) and ankerite ($(Ca,Fe)CO_3$) (Fig. 12C). The group classified as dolomite has the following compositional range: $(Ca_{0.48–0.60}Mg_{0.15–0.39}Fe_{0.08–0.29})_{\Sigma 0.95–1.23}CO_3$. Another group is Ca-poor and is classified as Mg-rich siderite: $(Ca_{0–0.11}Mg_{0.04–0.45}Fe_{0.23–0.73})_{\Sigma 0.87–0.99}CO_3$. Minor Mn (0.015–0.060 apfu) occurs in dolomite and Mg-rich siderite and is found proximal to the mineralization (in Sequence 2 rocks), although some carbonates in this setting show Mn contents below the detection limit or near zero concentrations. Pure calcite is the least common of the observed carbonate phases.

Chlorite: Chlorite composition was calculated on the basis of 14 oxygens and assuming all iron to be Fe^{2+}. All analyzed chlorite grains are from samples of the altered felsic lithofacies. The compositional range of the 56 analyzed grains is $(Al_{1.18–2.76}Fe_{1.01–2.97}Mg_{0.61–2.72})_{\Sigma 4.96–6.04}$ $(Si_{2.60–3.89}Al_{0.11–1.38})_{\Sigma 4.00}$ O_{10} $(OH)_8$. The analyzed chlorites fall into two distinct groups based on the Si, Fe, and Mg content (Hey, 1954). The more

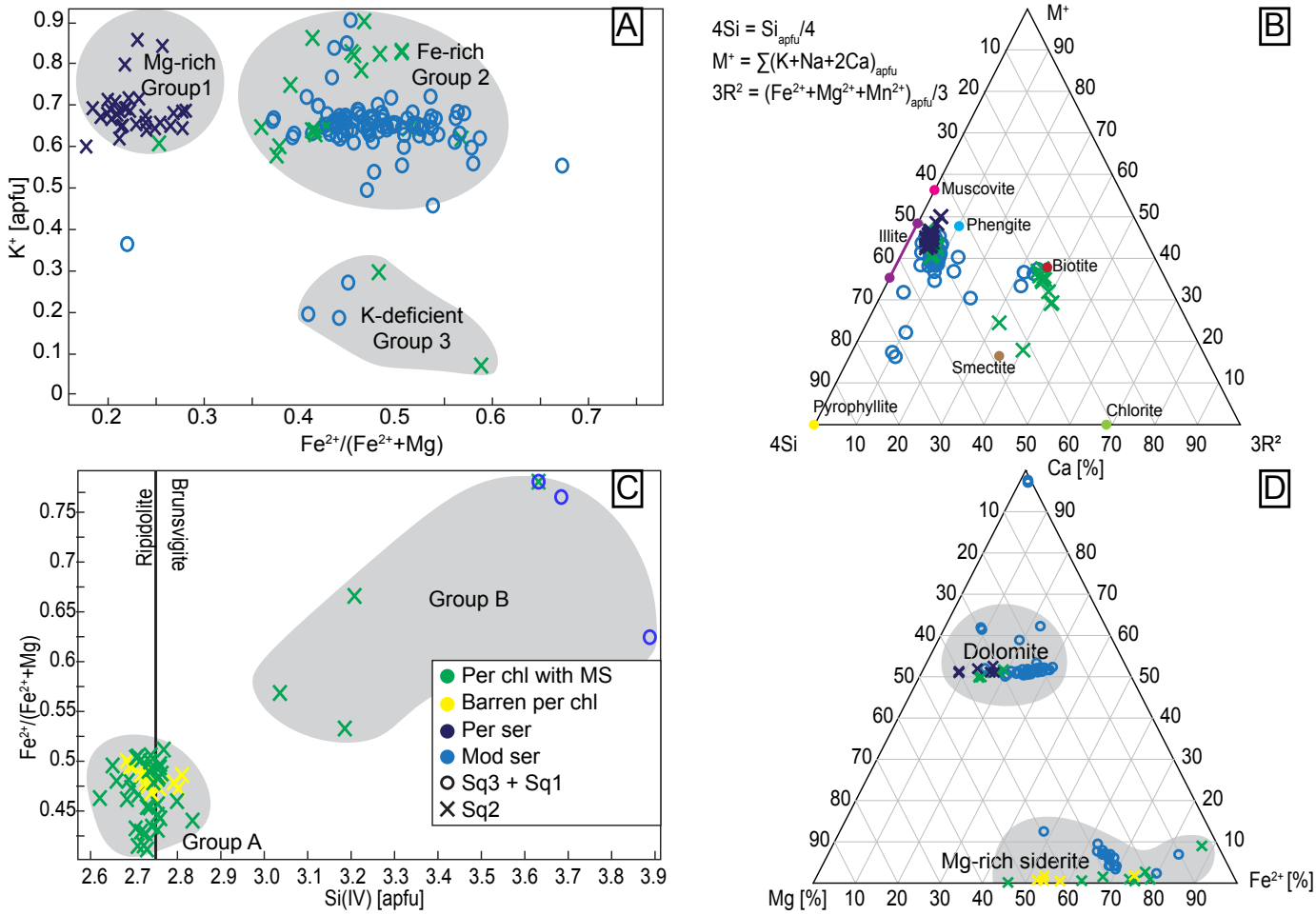

Fig. 12. Results of electron microprobe analysis (EMPA). A) Plot of $Fe^{2+}/(Fe^{2+} + Mg)$ vs. K^+ in atoms per formula unit (apfu) in white micas. B) 4Si-M + $3R^2$ diagram after Aja (2020) showing analyzed illite composition and ideal composition of phyllosilicates (Deer et al., 2013). C) Chlorite discrimination diagram after Hey (1954). D) Discrimination diagram for carbonates. Abbreviations: chl = chlorite, mod = moderate, MS = massive sulfide, per = pervasive, ser = sericite, Sq = sequence.

abundant group A occurs on the ripidolite-brunsvigite boundary; group B has a brunsvigite composition (Fig. 12C). The chlorites of group A are relatively homogeneous except for a minor subset that has elevated Mn content (~0.03–0.04 apfu) compared to group B. The Mn-rich samples occur within barren pervasive chlorite alteration that is not associated with massive sulfide mineralization.

Chlorite geothermometry: Geothermometry calculations were performed using the compositions of the 56 analyzed chlorite grains. Four methods were tested (Kranidiotis and MacLean, 1987; Cathelineau, 1988; Zang and Fyfe, 1995; Jowett, unpub. data), all based on calibrated empirical data and investigating the link between the contents of Al, Si, Fe, and Mg in chlorite in relation to temperature. All methods show that the calculated temperatures fall into two groups: the chlorites with compositions on the ripidolite-brunsvigite boundary formed at higher temperatures than the chlorites with the brunsvigite compositions (App. 5). Three of the methods (Kranidiotis and MacLean, 1987; Cathelineau, 1988; Jowett, unpub. data) report similar ranges of temperatures, with the lower-temperature group between 200° and 300°C and the higher-temperature group ranging between 300° and 400°C (App. 5). The last method (Zang and Fyfe, 1995) shows lower temperatures for both groups that are shifted approximately 100°C lower, but the method has not accounted for possible effects of pressure, whereas the other methods were developed using data from low-pressure environments, like the one presumed at the ABM deposit during its formation. We chose to report temperatures calculated according to Kranidiotis and MacLean (1987) because the ranges of calculated temperatures are closest to those expected based on the observed mineralization assemblages (chalcopyrite-pyrrhotite-pyrite-magnetite associated with chlorite ~350°C; Franklin et al., 2005; Hannington et al., 2005). Higher temperatures 322.0° ± 8.8°C (max 345°C; n = 49) characterize group A chlorites in the pervasive chlorite assemblage, whereas the lower-temperature chlorites occur in moderately sericite-altered felsic rocks (samples Q931984, Q930221; 134.2°C, n = 4) or as late minor chlorites occurring on sulfide grain boundaries in pervasively chlorite-altered rocks (sample Q721080; 243.4°C, n = 3).

Hyperspectral data

Results of the hyperspectral analyses of the samples (App. 6) show that the measured values of the 2200W wavelength span

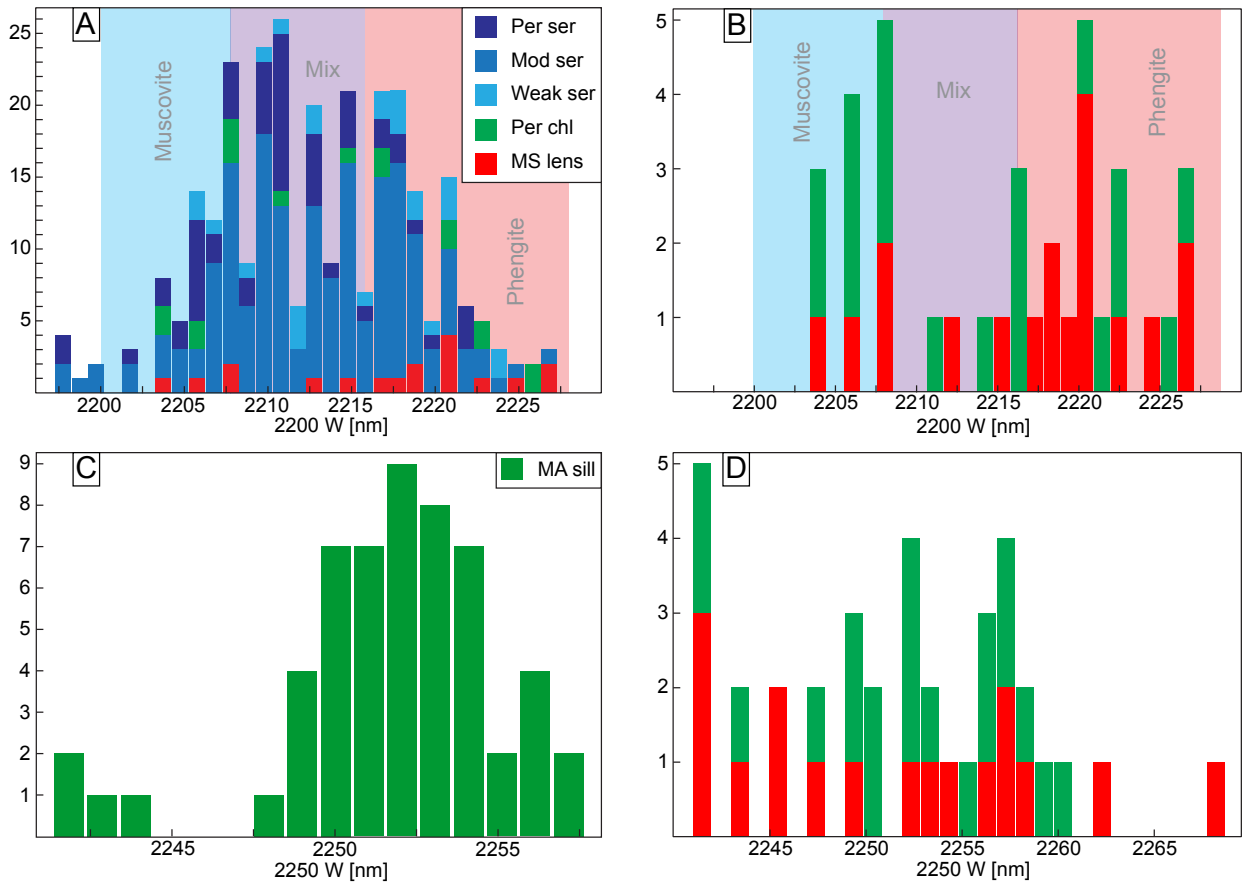

Fig. 13. Histograms showing results of short-wave infrared (SWIR) analyses. A) Values of 2,200-nm feature in felsic rocks. B) Values of 2,200-nm feature in pervasively chlorite altered and mineralized rocks. C) Values of 2,250-nm feature in mafic rocks with Mafic A (MA) signature. D) Values of 2,250-nm feature in pervasively chlorite-altered and mineralized rocks. Abbreviations: chl = chlorite, MA = Mafic A, MS = massive sulfide, per = pervasive, ser = sericite.

a wide range between 2,197 and 2,227 nm, largely independent of lithology (Fig. 4B). Felsic rocks with varying degrees of predominantly white mica alteration (pervasive to weak), both coherent and volcaniclastic, show a wide spread of values without any gaps (Fig. 13A). The relative abundance of values in the 2,208- to 2,216-nm range indicates the common occurrence of mixtures of the two white mica compositions—muscovite and phengite—within the alteration footprint. Only felsic samples with ΔK_2O >3% show 2200W feature values typical for phengite (2,215.5–2,224 nm). Mineralized or pervasively chlorite-altered samples (n = 54) show a bimodal distribution, with a gap in the 2,212- to 2217-nm range (Fig 13B). Proximal to the mineralization, values from the opposite sides of the 2200W feature spectrum commonly occur adjacent to each other over a few meters (Figs. 4, 10) regardless of lithology. The values of the depth of the 2200W feature are generally higher for felsic samples than for the mafic samples, indicative of more abundant white mica in the felsic rocks (Yang et al., 2011).

Values for the 2250W feature vary between 2,240 and 2,260 nm and do not correlate to any specific lithology. Felsic samples with no to low chlorite content, as recognized from drill core, commonly show values below 2,245 nm, which confirms the absence of chlorite in the rock (Herrmann et al., 2001). Mafic sill samples skew toward 2,250 nm feature values that are indicative of chlorite compositions with a higher Fe# compared to the other analyzed chlorites because most of the samples show values above 2,250 nm (Fig. 13C). Mafic sills with MA signatures show higher values for the depth of the 2250W feature, reflecting the abundant chlorite observed in thin sections compared to the sills with MB signatures that more commonly display lower abundances of chlorite and higher contents of biotite in thin section. Felsic samples displaying strong to pervasive chlorite alteration show a wide spread of values (Fig. 13D).

Compared with geochemical data, hyperspectral data for sericite-rich samples with longer 2200W feature wavelength values correspond to rocks with a higher Al_2O_3/Na_2O index and a higher K_2O content (Apps. 1, 6). The 2200W feature values do not correlate with AI, CCPI, or the Ba/Sr ratio. The 2250W feature correlates negatively with SiO_2 values in accordance with more abundant chlorite proportions observed in mafic and pervasively chlorite-altered rocks. Comparing values of the 2200W feature with averaged compositions of illite analyzed by the EMPA shows two groupings: samples with longer 2200W wavelengths (>2,213 nm) that represent the moderate sericite ± chlorite assemblage and have lower I (<0.7 apfu), higher Si/Al, and higher Fe# (>40%); and samples with shorter 2200W wavelengths (<2,208 nm) that have higher I and lower Si/Al values. One of the samples with

shorter 2200W wavelengths represents the pervasive sericite assemblage (D00005985) and has a low Fe# (<25%); the other sample (Q930221) represents the moderate sericite ± chlorite assemblage and has similar Fe# values (>40%). A possible reason for the shorter 2200W values in the latter sample is the presence of minor biotite in the sample. Samples representing the pervasive chlorite assemblage containing >40 modal % chlorite all have 2200W values >2,213 nm; illite from these samples has Fe# values >40%.

Discussion

In replacement-style VMS deposits, the contrasts in porosity and permeability within the subseafloor lithologies control hydrothermal fluid flow leading to irregular but mostly conformable alteration zones in the footwall and hanging wall of massive sulfide mineralization (Doyle and Huston, 1999; Doyle and Allen, 2003; Anderson et al., 2019; Nozaki et al., 2021). Despite past work in the Finlayson Lake district, there has been no study of the hydrothermal alteration footprint that has integrated field observations and mineralogical, spectral, and lithogeochemical data, and that relates the hydrothermal alteration to the emplacement mechanisms of the mineralization. Following brief remarks on the effects of greenschist facies metamorphism on hydrothermally altered rocks at the ABM deposit, the discussion will address two major topics: (1) how the hydrothermal system associated with the ABM deposit developed in time and space and its relation to the mineralization; and (2) what alteration vectors and at what scales they are the most useful to target a replacement-style VMS deposit in a dominantly felsic volcanosedimentary sequence.

Metamorphism in this part of the Finlayson Lake district reached a maximum of greenschist facies (Murphy et al., 2006). Generally, this metamorphic facies does not significantly affect the geochemical and mineral-chemical signatures produced by hydrothermal alteration, and recrystallized alteration-related phyllosilicates preserve their original premetamorphic compositions (Riverin and Hodgson, 1980; Urabe et al., 1983; Hannington et al., 2003; Genna and Gaboury, 2015). This appears to be the case at the ABM deposit; however, under contemporaneous deformation, the hydrothermally altered rocks at the ABM deposit recrystallized, which partially obscured the primary paragenetic relationships at the microscopic scale. The relationships between the different alteration assemblages on the deposit scale remain unaffected, as no major folding has been documented in the deposit footprint, the major deformation fabric is subparallel to primary bedding (van Olden et al., 2020), and the observed crosscutting relationships between alteration assemblages are not significantly affected by deformation. The effects of greenschist facies metamorpism are most apparent in the mafic sills in Sequence 2. The chlorite-carbonate-actinolite assemblage that occurs throughout this lithofacies contains locally abundant actinolite (Fig. 6A-B, D), which suggests it is of regional metamorphic origin (Arghe et al., 2011). Other overprinting minerals in the mafic sills are also linked to metamorphic processes (biotite, chlorite, zoned epidote; Fig. 6E-F). The effects of metamorphism on the mafic sills were likely isochemical, as samples of mafic sills affected by the chlorite-carbonate-actinolite assemblage plot mostly in the least-altered mafic rocks field in the alteration boxplot (Fig. 9C). Despite greenschist facies metamorphism and associated deformation in the ABM deposit, it does not significantly affect macro- and mesoscale relationships between hydrothermal alteration assemblages and/or host rocks, and the different mineral-chemical signatures of phyllosilicates and carbonates in hydrothermal alteration assemblages are also preserved. Thus, despite post-VMS metamorphism and deformation, the original footprint of VMS-related alteration and mineralization is still preserved and reflects the original evolution of the ABM deposit hydrothermal system and not subsequent post-VMS tectonothermal activity.

Hydrothermal system extent and evolution

Prior to VMS-related hydrothermal alteration (200°–350°C), the felsic volcanic rocks hosting the ABM deposit were likely affected by diagenetic alteration (<150°C) similar to the alteration processes described by Munhá et al. (1980) and Gifkins and Allen (2001). Evidence of these low-temperature (<200°C) prehydrothermal processes in the ABM deposit footprint is scarce, and these assemblages were predominantly overprinted by younger, higher-temperature hydrothermal alteration and post-VMS metamorphic assemblages. The paragenetically oldest observed alteration assemblage is recorded by the diagenetic trend in the felsic volcanic rocks on the alteration boxplot (Fig. 9C). This assemblage has a limited spatial distribution and comprises large (~0.5-cm) euhedral feldspar, most commonly albite. Similar zones of Na enrichment were described by Date et al. (1983) in the Kuroko district and recently by Pilote et al. (2019) in the Ming deposit, where this alteration assemblage was interpreted to form from late fluids generated by plagioclase breakdown or due to late influx of unmodified, cold, Na-rich seawater. Even though these zones of Na enrichment are locally associated with massive sulfide lenses at the ABM deposit, the euhedral feldspar crystals appear to be one of the earliest preserved phases, and locally, the feldspar is overprinted by white mica, chlorite, and/or carbonate along grain boundaries and fractures, implying its formation preceded pervasive VMS alteration. In the deposit area, the Na-rich alteration would have taken place during and after the deposition of Sequence 2 rocks and was succeeded by the higher-temperature VMS hydrothermal alteration (T > 230°C; Fig. 7).

The moderate sericite ± chlorite assemblage is the most spatially extensive hydrothermal alteration assemblage at the ABM deposit (Figs. 2-4), and it is the earliest of the higher-temperature assemblages as it is crosscut by all other VMS-related hydrothermal assemblages. The extent of the moderate sericite ± chlorite alteration assemblage, together with only rare later overprints further away from the core of the deposit (Fig. 2B), suggests that it formed as the initial phase of the hydrothermal fluid flow that infiltrated porous and permeable units where the hydrothermal fluids interacted with the host rocks saturated in cold seawater. The mapped moderate sericite ± chlorite alteration zones are stratabound and commonly flanked by units with lower porosities and permeabilities, such as coherent volcanic rocks or mudstones (Figs. 3-4). For such a widespread alteration halo to form away from the core of the hydrothermal system and the major synvolcanic faults, hydrothermal fluids must have circulated laterally through the units with high porosity and permeability (Large et al., 2001a;

Genna et al., 2014; Piercey et al., 2014), similar to what has been described in some modern-day SMS deposits (Anderson et al., 2019; Nozaki et al., 2021). Lateral flow of hydrothermal fluids within volcaniclastic units is further supported by the similarity of mica compositions along the extent of the moderate sericite ± chlorite alteration zones, which have 2200W feature spectral values that generally fall within the same range throughout the interpreted alteration lenses (Fig. 4). Commonly, the moderate sericite ± chlorite assemblage has 2200W values in the same range as the assemblage samples analyzed by EMPA that contain predominantly group 2 illite (2200W > 2,212 nm).

Mineral-chemical data from samples in moderate sericite ± chlorite alteration samples show there was voluminous early illite in this assemblage. Temperatures calculated using illite compositions from moderately sericite ± chlorite-altered zones average 214.5° ± 33.0°C (n = 110 from four samples). In hydrothermal systems, illite commonly forms in the early stages at lower temperature and/or at lower pH (Iijima, 1974; Schardt et al., 2001). Under such conditions, white mica forms preferentially over chlorite (Schardt et al., 2001), which would explain the relative scarcity of chlorite in the most widespread alteration assemblage in the ABM deposit. Where chlorite is more abundant in the moderate sericite ± chlorite assemblage (~10 modal % and above), it is likely due to more extensive mixing of hydrothermal fluids with the seawater present in the water-saturated porous and permeable units, which would have raised the pH of the fluid, added Mg, and would have allowed chlorite to precipitate (Schardt et al., 2001). Proximal to zones of pervasive sericite alteration, disseminated sulfides occur within the moderate sericite ± chlorite assemblage. In other VMS deposits, pyrite is a common component of sericite alteration assemblages forming at temperatures below 250°C (Schardt et al., 2001), which correlates with the proposed temperatures at which the alteration minerals composing this alteration assemblage formed.

In VMS deposits, zones of pervasive alteration are interpreted to be the pathways of the most intense fluid flow with highest fluid/rock ratios and highest fluid temperatures (e.g., Holk et al., 2008). The center of the ABM deposit comprises zones of pervasive alteration that surround the mineralized bodies and overprint the moderate sericite ± chlorite alteration assemblage. The temperatures recorded by group 1 illite in pervasive sericite altered zones here are 248.9° ± 14.9°C, similar to temperatures recorded in pervasive sericite zones in other VMS deposits (Schardt et al., 2001). A lens of moderately to pervasively green mica-sericite–altered felsic volcaniclastic rocks occurs between the two mafic sills in Sequence 2 (Fig. 4). This alteration assemblage has elevated Cr content (~600 ppm) compared to other felsic volcanic rocks (<30 ppm Cr) and occurs at or in proximity to mafic sill contacts, which are inferred to be the source of Cr for the green mica, as mafic sills with MA signatures contain high Cr values (>290 ppm Cr; Denisová and Piercey, 2022). Intense fuchsite-carbonate-barite alteration has been described in basalts directly in the hanging wall of the Hellyer deposit, Tasmania, and the source of Cr in fuchsite was determined to be the breakdown of Cr-rich pyroxenes in the basalt (Gemmell and Large, 1992; Large et al., 2001c); mafic rocks were likely the source of Cr in the ABM deposit as well. At the ABM deposit, the lens of green mica-altered rocks is interpreted to mark a zone of maximum fluid flow in the restricted space below the massive sulfide lenses and between the mafic sills. Temperatures calculated for mica in the pervasive sericite alteration zones at the ABM deposit (248.9° ± 14.9°C) are in a similar range as those reported for the fuchsite alteration zone at Hellyer (~250°C; Gemmell and Fulton, 2001). Proximal to the mineralization, temperatures calculated from chlorite compositions in pervasively chlorite-altered zones, both mineralized and barren, are ~315° ± 30°C, which are typical for chlorite alteration in VMS deposits, globally (Kranidiotis and MacLean, 1987; Mercier-Langevin et al., 2014). Textural relationships show that pervasive chlorite alteration overprints pervasive sericite alteration (Fig. 5F), and that sulfide mineralization overprints all types of pervasive alteration (Fig. 8), although locally massive sulfide mineralization is interpreted to be contemporaneous with the pervasive chlorite alteration. Additionally, in the pervasive chlorite alteration associated with the massive sulfide lenses, one of the earliest occurring ore minerals is magnetite, which commonly occurs spatially associated with chalcopyrite and pyrrhotite, indicative of formation from >350°C high-temperature fluids (Franklin et al., 2005; Hannington et al., 2005), which is consistent with the formation temperature calculated for chlorites above. These relationships between alteration and ore mineral assemblages suggest a steady rise in temperatures of the hydrothermal fluids culminating in the precipitation of massive sulfide mineralization in Sequence 2.

The occurrence of pervasive sericite and moderate sericite ± chlorite assemblages in Sequence 3 in the hanging wall of the massive sulfide lenses (Fig. 3, 4) indicates that the hydrothermal system was active after the main mineralization phase ended in Sequence 2. These hanging-wall alteration zones likely formed during the shorter breaks in volcanic activity recorded by lesser argillite lenses present throughout Sequence 3 (Denisová and Piercey, 2022) and are not associated with significant mineralization (Figs. 3, 4). The lack of overprinting of the mineralization by further pervasive hydrothermal alteration suggests that the hydrothermal fluids responsible for the alteration assemblages in the hanging wall exploited a different part of the synvolcanic fault/conduit network. These pathways were still relatively proximal to the mineralized part of the hydrothermal system due to the occurrence of the pervasive sericite assemblage in the hanging wall, but their more limited extent downdip (Fig. 3) suggests that their source could have occurred to the south of the current outcrop of the massive sulfide mineralization at the bedrock surface. Further, alteration intensity of the sericite ± chlorite assemblage in Sequence 3 varies from moderate to weak with distance from the mineralization, suggesting a decrease in intensity of hydrothermal fluid flow distal from the upflow zones.

The hanging wall in Sequence 3 also contains the greatest abundance of K-deficient illite/smectite (group 3) in the deposit. Within Sequence 3, the group 1 and group 2 illites found in the pervasive and moderate assemblages are overgrown by minor K-deficient illite/smectite (group 3). These group 3 illite/smectite grains also overprint the Sequence 2 mineralized and pervasively chlorit- altered zones, implying that they are very late in the evolution of the ABM hydrothermal system. The group 3 illite/smectite has average calculated formation temperatures of 110.4° ± 14.6°C (n = 4 from two

samples), implying a further cooling of the hydrothermal system as it evolved.

These assemblages are also crosscut by widespread Mg-rich siderite (vs. diagenetic dolomite), which occurs as coatings and overprints on other alteration phases throughout the upper Kudz Ze Kayah formation and up into the Wind Lake formation. This late Fe carbonate overprint is interpreted to reflect a very late, low-temperature phase of the hydrothermal system, likely formed through low-temperature diffuse venting at the sea floor, similar to the Wolverine deposit (Bradshaw et al., 2008).

The complexity of the observed overprinting of alteration and mineralization assemblages in the ABM deposit demonstrates that the deposit formed via an evolving hydrothermal system that comprised multiple pulses of fluids at varying temperatures. This is not unique to the ABM deposit, as similar style alteration assemblages and mineralization have been discovered at the base of the Kudz Ze Kayah formation in the GP4F deposit (Boulton, 2002), the R15 deposit (MacRobbie and Holroyd, unpub. data), and several anomalous showings across the stratigraphy (van Olden et al., 2020). This suggests that hydrothermal activity was ongoing throughout the deposition of the Kudz Ze Kayah formation and that conditions favourable for the precipitation of mineralization were not limited to a single horizon within the Kudz Ze Kayah formation, implying that there is potential for mineralization in other portions of the stratigraphy.

VMS mineralization vectoring

The hydrothermal alteration footprint of VMS mineralization is relatively small on the scale of a VMS district (100s to low 1,000s of meters; Sangster, 1980). Therefore, successful exploration for VMS deposits requires the use of complimentary geologic, geochemical, and mineralogical vectors to track the footprint of hydrothermal processes involved in formation of massive sulfide mineralization (Hannington et al., 2003; Gibson et al., 2007). Further, hydrothermal alteration in replacement-style VMS deposits is complex, in large part due to the more widespread infiltration of the hydrothermal fluids into host rocks in the subseafloor environment (Gibson et al., 1999; Doyle and Allen, 2003). In the following section, we will describe geochemical and mineralogical vectors within the ABM deposit from distal to proximal to the mineralization and link them to the VMS-related hydrothermal processes, utilizing whole-rock mobile major and trace mobile elements, and mineral chemistry, to determine alteration intensity variations with proximity to massive sulfide mineralization.

The most widespread hydrothermal alteration assemblages at the ABM deposit are the weak- to moderate-intensity hydrothermal alteration zones in the upper Kudz Ze Kayah formation that envelop the ABM and Krakatoa mineralized zones and several prospective base metal anomalies. The combination of alteration and overprinting sulfide mineralization result in distinctive chemical and mineral-chemical changes. As with most VMS deposits, feldspar destruction and subsequent formation of phyllosilicate minerals (white mica ± chlorite) had resulted in very low absolute concentrations and mass losses of Na_2O (Fig. 11A) and high Spitz-Darling index values (Fig. 9D; Spitz and Darling, 1978; MacLean and Barrett, 1993; Barrett and MacLean, 1994a) across the ABM deposit footprint. The lateral continuity of the zones affected by weak- to moderate-intensity alteration can be tracked through the mineral chemistry of the phyllosilicate minerals. Similar conditions (pH, redox, temperature) within these zones produced illites with homogeneous compositions that can monitored using mineral chemistry or the 2200W feature (Figs. 4, 12A, C).

Barium is also a district- to deposit-scale vector towards massive sulfide mineralization. Denisová and Piercey (2022) noted that Ba >3,500 ppm is indicative of pervasive sericite alteration assemblages proximal to mineralization and extending into the hanging wall and was useful in mapping the likely lateral flow in the deposit (Fig. 4). White mica in these Ba-rich zones also exhibits minor but elevated Ba content including in the hanging wall of the mineralization. Given that these Ba-rich micas are contemporaneous with to slightly after sulfide formation (Fig. 7), it is possible they received Ba via dissolution of barite during the precipitation of early, high-temperature sulfide mineralization (e.g., Magnall et al., 2020). Equally viable, however, is that they could be related to upwelling Ba-rich hydrothermal fluids that have been recognized in other VMS districts (e.g., Lentz et al., 1997). The Ba-bearing micas are restricted to the ABM deposit and have limited extent within the deposit footprint (e.g., 10s to 100s of meters), unlike other VMS districts (Hannington et al., 2003), but absolute Ba values can be used for district-scale vectoring.

Although Ba and Na_2O variations are useful for both regional- and deposit-scale vectoring, other elements are more spatially sensitive and richer closer to the mineralization. In areas proximal to the massive sulfide mineralization (<200 m), zones of pervasive sericite alteration assemblages with extensive formation of sericite translate to mass gains of K_2O (Fig. 11B) and elevated Ishikawa alteration index values (Fig. 9C). Increasing absolute values and mass gains of K_2O reflect progressively more pervasive sericite alteration and can be used to vector toward zones of highest intensity alteration. In most VMS environments, high Ba/Sr and Rb/Sr indices are also useful vectors for sericite alteration and Ba enrichment (Large et al., 2001a; McNulty et al., 2020) because they monitor both feldspar destruction and phyllosilicate formation in a similar way to K_2O-Na_2O-CaO systematics. Strontium substitutes for Ca, and Ba or Rb substitute for K in various primary and alteration phases (Large et al., 2001a). At the ABM deposit, Ba increases with proximity to mineralization (Denisová and Piercey, 2022), but it is not accompanied by coincident low Sr values due to the presence of overprinting carbonate alteration, which leads to Sr enrichment and mixed Ba/Sr ratios throughout the deposit. In contrast, the Ba/Na_2O ratio tracks similar processes as the Ba/Sr ratio, correlates well with AI, Al_2O_3/Na_2O, and other monitors of hydrothermal alteration discussed below, and can be used on a district scale (km-scale) to delineate VMS-prospective rocks.

Proximal to the mineralization (<200 m), elevated values of base and trace metals occur in the host rocks. Mass balance calculations show mass gains of Zn, Pb, Cu, and Ba with proximity to the mineralization (Fig. 11D-F). Additionally, elements commonly enriched in massive sulfides, such as Tl, Sb, As, Ag, Cd, Mo, Bi, and Se, have anomalous values in altered felsic rocks and increase in concentration with proximity to the mineralized lenses (Fig. 10), whereas Co and Ni decrease. The altered rocks commonly contain disseminated sulfides,

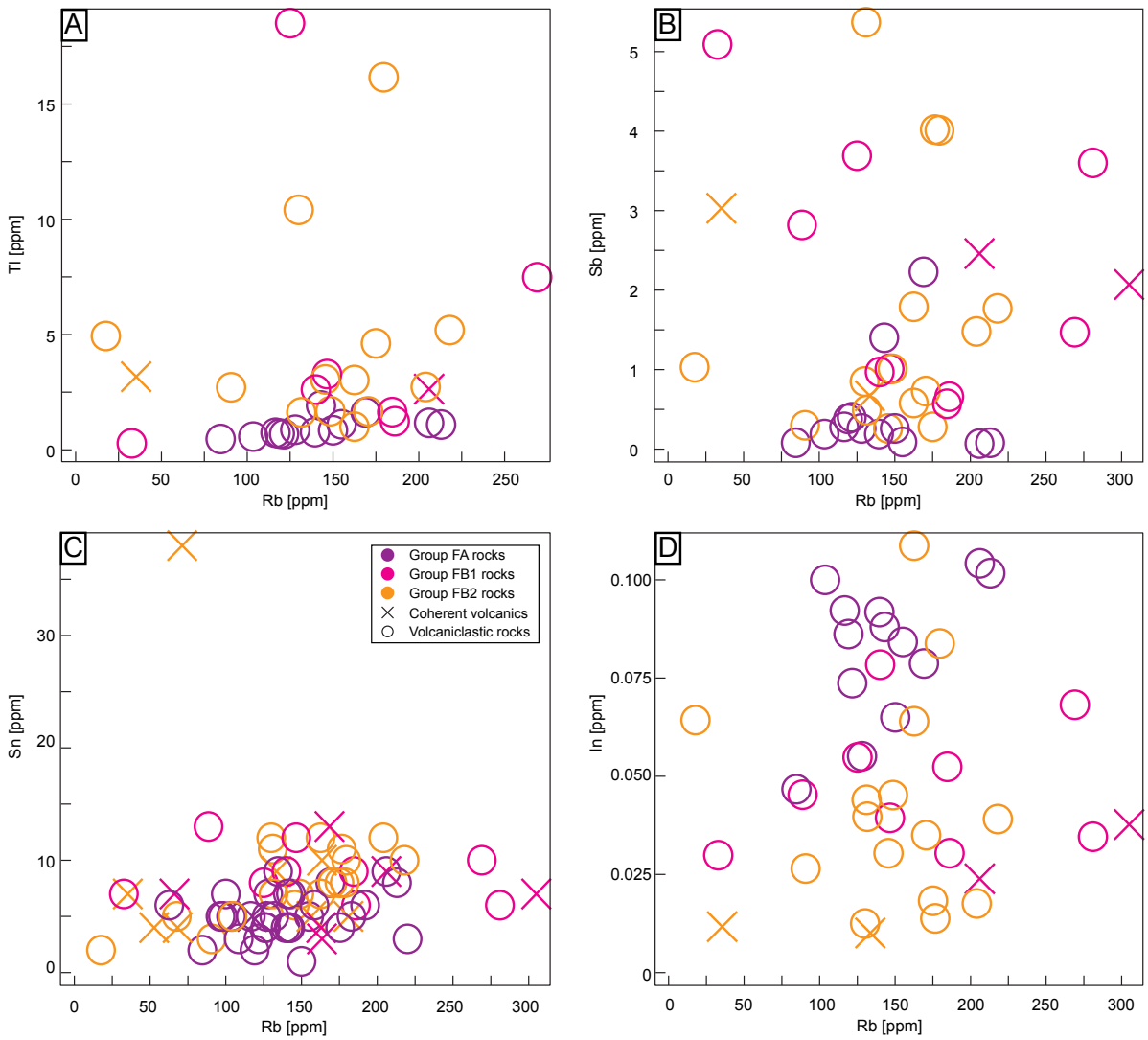

Fig. 14. Plots of Rb versus trace elements in felsic rocks. Rb stands in for K_2O. A) Rb vs. Tl. B) Rb vs. Sb. C) Rb vs. Sn. D) Rb vs. In. Abbreviations: CCPI = chlorite-carbonate-pyrite index, FA = Felsic A, FB = Felsic B..

and it is likely they carry some of these trace metals proximal to the massive sulfide mineralization. Soltani Dehnavi et al. (2018) have also shown that semivolatile metals like Tl, Sb, Sn, Hg, and In can exhibit lithophile behavior and be hosted in phyllosilicates like mica and chlorite. Whole-rock data for felsic rocks shows correlation between Rb (substituting for K) and Tl, Sn, In, and Sb (Fig. 14), suggesting that, at least distal from the mineralization in Sequence 1 and 3 in moderately altered felsic rocks, these semivolatile metals likely occur in micas, which extends the trace element halo further away from the massive sulfide mineralization. This is further supported by comparing the results from different digestion methods (HF-HCl-$HClO_4$ digest vs. aqua regia digest) used for geochemical analysis of the felsic samples (Fig. 15). The aqua regia digestion dissolves sulfides and other weakly resistant minerals, whereas the HF-HCl-$HClO_4$ solution digests the majority of silicates present in the sample. In the case of semivolatile metals (Tl and Sb), if values from the different digests match, the metals likely occur in sulfides. If the results are higher for the HF-HCl-$HClO_4$ digest, it is likely that the metals are occurring in silicates, most likely phyllosilicates like white mica or chlorite. The results demonstrate that Tl is likely hosted by silicate minerals, as the analyses of felsic samples skew toward higher concentrations in the HF-HCl-$HClO_4$ digest (Fig. 15). Based on this, Tl, either as absolute values or in a ratio with Co (Genna and Gaboury, 2019), can be used to map sericite alteration and its intensity in felsic lithofacies of the upper Kudz Ze Kayah formation (Figs. 9, 10, 15).

The most proximal alteration in the ABM deposit is the pervasive chlorite alteration that is closely associated with massive sulfide mineralization (<50 m) and is characterized by high values of the chlorite-carbonate-pyrite and Ishikawa alteration indices (Fig. 9C) and by mass gains of MgO and FeO and mass losses of K_2O and SiO_2 (Fig. 11B-C). Such features are typical for chlorite forming at the expense of feldspar and white mica (Barrett and MacLean, 1994b; Schardt et al., 2001). In contrast to zones of strong to pervasive sericite alteration, zones of pervasive chlorite alteration at the ABM deposit show Ba values below the 3,500-ppm threshold. This likely indicates that the hydrothermal fluids associated with

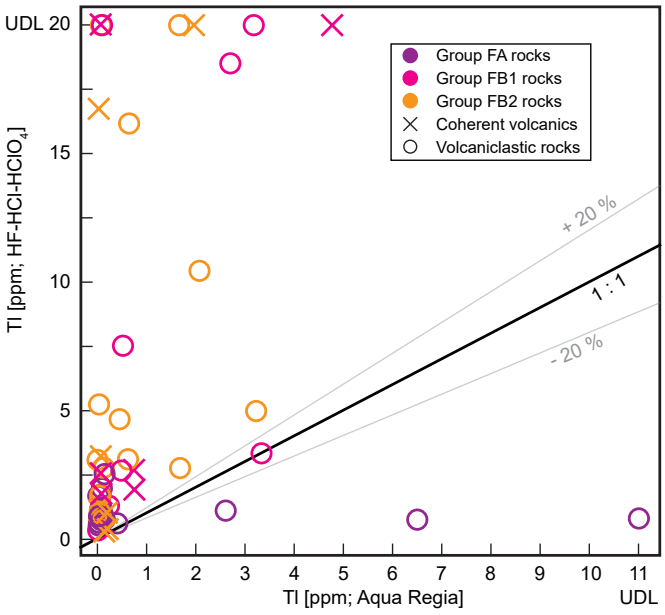

Fig. 15. Comparison of trace element results in felsic rocks using the aqua regia and HF-HCl-$HClO_4$ digests in sample analysis. The HF-HCl-$HClO_4$ digests the majority of minerals, aqua regia leaches loosely bound elements and digests sulfides, Fe and Mn oxides, sulfates, carbonates, and some silicates. A) Comparison of digestions for Tl; Tl likely more prevalent in silicates. Detection range of Tl in aqua regia is between 0.0006 and 11 ppm; in HF-HCl-$HClO_4$, it is between 0.002 and 20 ppm. B) Comparison of digestions for Sb; Sb can occur both in silicates and less resistant minerals, likely sulfides. Detection range of Sb in aqua regia is between 0.009 and 5,500 ppm; in HF-HCl-$HClO_4$, it is between 0.04 and 28 ppm. FA = Felsic A, FB = Felsic B.

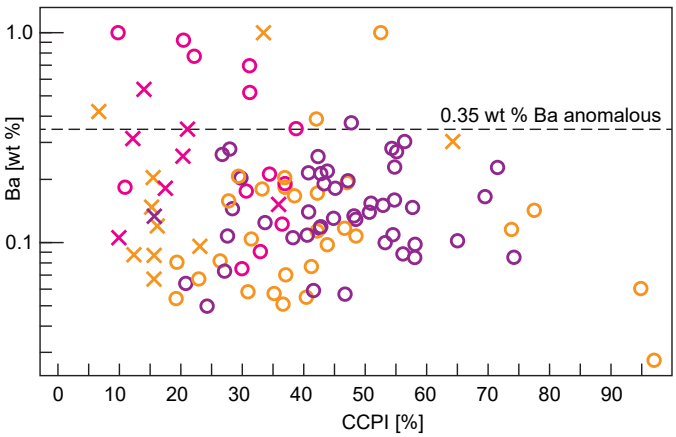

Fig. 16. Plot of chlorite-carbonate-pyrite index (CCPI) vs. Ba in felsic rocks, the threshold for anomalous Ba values (0.35 wt %) marked in plot.

zones of pervasive chlorite alteration were reduced, acidic, and high temperature (~320°C) and dissolved any barite present and/or remobilized any Ba present into feldspars and micas (± carbonates; Fig. 16; Cooke et al., 2000). Chlorite in mineralized or mineralization-proximal pervasive alteration zones is more Mg rich than chlorite from distal, moderately sericite ± chlorite-altered zones (Fig. 12C). In these proximal Mg-chlorite–rich zones, the illite composition behaves similarly, and illite is enriched in Mg proximal to mineralization (Fig. 12A), which has been observed in some VMS districts (e.g., Skellefte district; Hannington et al., 2003; Chmielowski et al., 2016). This Mg enrichment was interpreted to be due to abundant entrained Mg-rich seawater mixing with the hydrothermal fluids, whereas the sulfides precipitated later without significant input of seawater and Mg enrichment (Hannington et al., 2003; Chmielowski et al., 2016). Another possible explanation is that early in the evolution of the hydrothermal system, Fe from the hydrothermal fluids was consumed by precipitation of Fe-rich sulfides or magnetite, whereas the consequently more Mg-rich fluid precipitated the more Mg-rich phyllosilicates (Richards et al., 1989; Saccocia and Seyfried, 1994). Given the strong association of Mg-rich chlorite with proximity to mineralization, the latter explanation is the more plausible for Mg-rich chlorite formation.

At the ABM deposit, gradients in lithogeochemical and mineral-chemical data are observed on a regional scale, including those reflecting feldspar destruction (e.g., Na_2O, mass changes of Na_2O, K_2O, Spitz-Darling index) and enrichments in elements hosted by alteration minerals and sulfides (e.g., Ba, base metals, gradients in Fe-Mg contents of phyllosilicates). To delineate and vector toward zones proximal to mineralization, tracking of coincident geochemical indicators (AI > 80, CCPI > 65, Ba/Na_2O > 1), changes in mass balance of major elements (mass gains of K_2O, MgO, FeO, Ba, mass losses of Na_2O) and base metals (mass gains of Zn, Cu, Pb), mineral chemistry of phyllosilicates (Mg-rich compositions, enrichments in Ba and/or trace metals proximal to VMS), increase in base (Zn, Cu, Pb) and trace metal (Sb, Tl, Mn, In, Sn, Mo) values, and SWIR features typical for certain phyllosilicate compositions (specific illite composition in sericite-bearing alteration assemblages) should accompany detailed field mapping of alteration and alteration intensity (Fig. 17).

Conclusion

At least two major alteration episodes are recorded in the host rocks of the ABM deposit. Early diagenesis-related alteration is preserved locally in Sequence 2, whereas extensive hydrothermal alteration affected most of the rocks in the ABM deposit footprint, with the distribution of alteration zones being controlled by the porosity and permeability contrasts between coherent and volcaniclastic/sedimentary units. Within the core of the hydrothermal alteration at the ABM deposit, there are zones of pervasive alteration that envelop lenses of massive sulfide mineralization, with lower-temperature assemblages (pervasive sericite or moderate sericite ± chlorite alteration) overprinted by higher-temperature assemblages (pervasive chlorite alteration). The hydrothermal system that formed the ABM deposit was at its peak during the volcanic hiatus between the deposition of Sequence 2 and Sequence 3; this hiatus was also when mineralization and pervasive alteration in Sequence 2 were formed. The hydrothermal system continued post-VMS formation and involved pervasive sericite and moderate to weak sericite ± chlorite alteration extending up to 300 m into the hanging wall of the massive sulfide mineralization, implying that the hydrothermal system was active during the deposition of the volcanic rocks of Sequence 3.

The most extensive zones of hydrothermal alteration at the ABM deposit extend laterally up to 1,000 m along strike from mineralization and are concentrated along originally porous

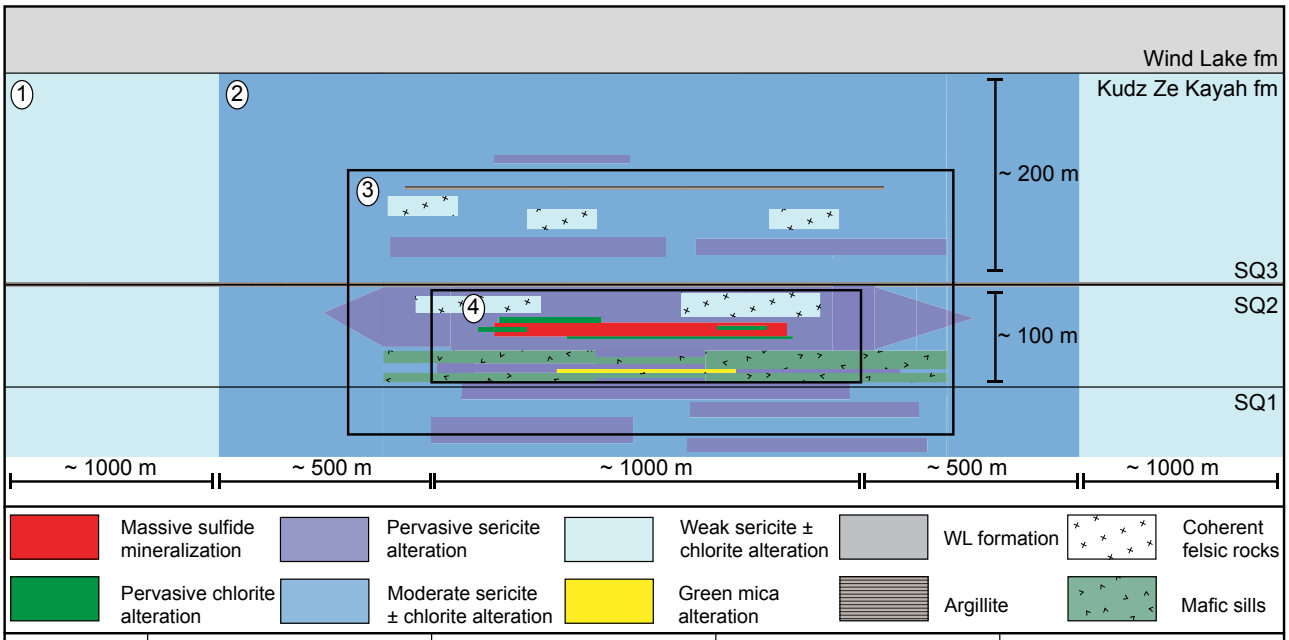

	Distal weak (1)	Distal moderate (2)	Proximal (3)	Proximal MS (4)
Spitz-Darling	>5	>10	>20	>20
AI	n/a	>65%	>80%	>80%
CCPI	n/a	n/a	n/a	>65%
Mass balance	$\Delta Na_2O << 0$, $\Delta K_2O > 0$	$\Delta K_2O >> 0$, $\Delta Na_2O << 0$	$\Delta K_2O >> 0$, $\Delta Na_2O << 0$	ΔK_2O, ΔMgO, $\Delta FeO >> 0$
Ba/Na_2O	n/a	>0.5	>1	n/a
Ba [wt %]	~0.15%	~0.15%	>0.35%	>0.35%
Rb [ppm]	n/a	>100	>150	>150
Fe# mica	>0.3	>0.3	<0.3	<0.3
Fe# chlorite	n/a	>0.5	>0.5	<0.5
Base metals	n/a	Cu < 30 ppm, Pb < 20 ppm, Zn < 100 ppm	Cu >30 ppm, Pb > 70 ppm, Zn > 200 ppm	n/a
Tl [ppm]	n/a	>1	>1	>>1
Sb [ppm]	n/a	>1	>1	>>1
Mn [ppm]	n/a	>0.075	<0.075	n/a
In [ppm]	n/a	>0.06	<0.06	n/a
2200W [nm]	<2208	>2212	>2216	<2208 and >2216

Fig. 17. Simplified stratigraphy of the upper Kudz Ze Kayah formation showing schematic distribution of the hydrothermal alteration assemblages at the ABM massive sulfide deposit. Approximate values of key alteration indices and minor and trace elements characteristic for the main hydrothermal alteration assemblages are shown in the accompanying table. Abbreviations: AI = Ishikawa alteration index, CCPI = chlorite-carbonate-pyrite index, MS = massive sulfide mineralization.

and permeable units within the volcanosedimentary package. Quantifying feldspar destruction identifies these broad zones of weak to moderate alteration. Precipitation of minor disseminated sulfides within zones of moderate and pervasive alteration also resulted in enrichment in base and trace metals (Zn, Cu, Pb, Ag, Au, Mo, Sb, Tl, As, Hg) in proximity to massive sulfide mineralization (<200 m). The composition of phyllosilicate minerals characteristic for the moderate and pervasive alteration assemblages is dependant on the temperature at which they formed, and they are more Mg-rich and K-rich proximal to massive sulfide mineralization, where the hydrothermal fluids had the highest temperatures. They can also be enriched in minor and trace metals (Ba, Rb, Tl, Sb). Mineral chemistry and SWIR spectroscopy can both be used to identify compositional vectors from the distal parts of the alteration footprint toward massive sulfide mineralization and to track the lateral continuity of the zones affected by different hydrothermal alteration assemblages. Notably, there are complex overprinting alteration mineral relationships reflecting the evolution of the dynamic hydrothermal system at the ABM deposit, demonstrating that SWIR spectral signals are challenging to interpret in such dynamic systems, and sound interpretation of such data requires good control on alteration mineral paragenesis and relationships to mineralization.

Acknowledgments

We would like to thank BMC Minerals Ltd. for their generous financial, field, and logistical support. Support for the project was provided by grants from the NSERC Discovery Grant, the NSERC Collaborative Research Development Grant – Project (CRDPJ) program, and BMC Minerals Ltd. (Piercey), a Student Research Grant from the Society of Economic Geologist Canada Foundation, and by funding from Memorial University of Newfoundland (Denisová). We thank Dr. Wanda Aylward for her assistance with analytical work. We thank Dr. Stefanie Brueckner, Dr. Nils Jansson, and Associate Editor Dr. Jonathan Cloutier for their thorough reviews of the manuscript that improved it greatly. The corresponding author would like to thank Matthew Manor and Rose Cobbett for constructive comments on an earlier draft of the manuscript, Neil Martin and Robin Black from BMC Minerals, Dillon Hume from Equity Exploration, and Robert Burke for helpful comments and conversations beneficial to this paper. We thank BMC Minerals and Equity Exploration staff at the Kudz Ze Kayah exploration camp for their help during the 2018 and 2019 field seasons.

REFERENCES

Aja, S.U., 2020, On the thermodynamic stability of illite and I-S minerals: Clays and Clay Minerals, v. 67, p. 518–536.

Anderson, M.O., Hannington, M.D., McConachy, T.F., Jamieson, J.W., Anders, M., Wienkenjohann, H., Strauss, H., Hansteen, T., and Petersen, S., 2019, Mineralization and alteration of a modern seafloor massive sulfide deposit hosted in mafic volcaniclastic rocks: Economic Geology, v. 114, p. 857–896.

Arghe, F., Skelton, A., and Pitcairn, I., 2011, Spatial coupling between spilitization and carbonation of basaltic sills in SW Scottish Highlands: Evidence of a mineralogical control of metamorphic fluid flow: Geofluids, v. 11, p. 245–259.

Barrett, T.J., and MacLean, W.H., 1994a, Chemostratigraphy and hydrothermal alteration in exploration for VHMS deposits in greenstones and younger volcanic rocks: Geological Association of Canada, Short Course Notes, v. 11, p. 433–467.

——1994b, Mass changes in hydrothermal alteration zones associated with VMS deposits of the Noranda area: Exploration and Mining Geology, v. 3, p. 131–160.

Barrett, T.J., Cattalani, S., and MacLean, W.H., 1993, Volcanic lithogeochemistry and alteration at the Delbridge massive sulfide deposit, Noranda, Quebec: Journal of Geochemical Exploration, v. 48, p. 135–173.

Barrett, T.J., Dawson, G.L., and MacLean, W.H., 2008, Volcanic stratigraphy, alteration, and sea-floor setting of the Paleozoic Feitais massive sulfide deposit, Aljustrel, Portugal: Economic Geology, v. 103, p. 215–239.

Battaglia, S., 2004, Variations in the chemical composition of illite from five geothermal fields: A possible geothermometer: Clay Minerals, v. 39, p. 501–510.

Boulton, A., 2002, GP4F polymetallic volcanic-hosted massive sulphide (VHMS) deposit, Finlayson Lake district, Yukon Territory: B.Sc. thesis, Victoria, British Columbia, University of Victoria, 56 p.

Bradshaw, G.D., Peter, J.M., Paradis, S., and Rowins, S., 2001, Geological characteristics of the Wolverine volcanic-hosted massive sulphide deposit, Finlayson Lake district, Yukon Territory, Canada, *in* Emond, D.S., and Weston, L.H., eds., Yukon Exploration and Geology: Yukon Geologicla Survey, p. 269–288.

Bradshaw, G.D., Rowins, S.M., Peter, J.M., and Taylor, B.E., 2008, Genesis of the Wolverine volcanic sediment-hosted massive sulfide deposit, Finlayson Lake district, Yukon, Canada: Mineralogical, mineral chemical, fluid inclusion, and sulfur isotope evidence: Economic Geology, v. 103, p. 35–60.

Brueckner, S.M., Johnson, G., Wafforn, S., Gibson, H.L., Sherlock, R., Anstey, C., and Mcnaughton, K., 2021, Potential for volcanogenic massive sulfide mineralization at the A6 Anomaly, north-west British Columbia, Canada: Stratigraphy, lithogeochemistry, and alteration mineralogy and chemistry: Minerals, v. 11, 50 p.

Burnham, O.M., 2008, Trace element analysis of geological samples by inductively coupled plasma mass spectrometry (ICP-MS) at the Geoscience Laboratories: Revised capabilities due to method improvements: Summary of field work and other activities: Ontario Geological Survey, Open File Report 6226, p. 1–10.

Burnham, O.M., and Schweyer, J., 2004, Trace element analysis of geological samples by inductively coupled plasma mass spectrometry at the Geoscience Laboratories: Revised capabilities due to improvements to instrumentation: Summary of field work and other activities: Ontario Geological Survey, Open File Report 6145, p. 1–20.

Buschette, M.J., and Piercey, S.J., 2016, Hydrothermal alteration and lithogeochemistry of the Boundary volcanogenic massive sulphide deposit, central Newfoundland, Canada: Canadian Journal of Earth Sciences, v. 53, p. 506–527.

Cathelineau, M., 1988, Cation site occupancy in chlorites and illites as a function of temperature: Clay Minerals, v. 23, p. 471–485.

Chmielowski, R.M., Jansson, N.F., Persson, M.F., and Fagerström, P., 2016, 3D modeling of hydrothermal alteration associated with VHMS deposits in the Kristineberg area, Skellefte district, northern Sweden: Mineralium Deposita, v. 51, p. 113–130.

Cloutier, J., and Piercey, S.J., 2020, Tracing mineralogy and alteration intensity using the spectral alteration index and depth ratios at the Northwest zone of the Lemarchant volcanogenic massive sulfide deposit, Newfoundland, Canada: Economic Geology, v. 115, p. 1055–1078.

Cloutier, J., Piercey, S.J., and Huntington, J., 2021, Mineralogy, mineral chemistry and SWIR spectral reflectance of chlorite and white mica: Minerals, v. 11, 16 p.

Colpron, M., Nelson, J.L., and Murphy, D.C., 2006, A tectonostratigraphic framework for the pericratonic terranes of the northern Canadian Cordillera: Geological Association of Canada, Special Paper 45, p. 1–23.

Cooke, D.R., Bull, S.W., Large, R.R., and McGoldrick, P.J.. 2000, The importance of oxidized brines for the formation of Australian Proterozoic stratiform sediment-hosted Pb-Zn (Sedex) deposits: Economic Geology, v. 95, p. 1–18.

Date, J., Watanabe, Y., and Saeki, Y., 1983, Zonal alteration around the Fukazawa Kuroko deposits, Akita prefecture, northern Japan: Economic Geology Monograph 5, p. 365–386.

Davies, J.F., and Whitehead, R.E., 2006, Alkali-alumina and MgO-alumina molar ratios of altered and unaltered rhyolites: Exploration and Mining Geology, v. 15, p. 75–88.

Deer, W.A., Howie, R.A., and Zussman, J., 2013, An introduction to the rock-forming minerals, 3rd ed.: London, Mineralogical Society of Great Britain and Ireland, 498 p.

Denisová, N., and Piercey, S.J., 2022, Lithostratigraphy, lithogeochemistry, and tectono-magmatic framework of the ABM replacement-style volcanogenic massive sulfide (VMS) deposit, Finlayson Lake district, Yukon, Canada: Economic Geology, v. 117, p. 1299–1326.

Doyle, M.G., and Allen, R.L., 2003, Subsea-floor replacement in volcanic-hosted massive sulfide deposits: Ore Geology Reviews, v. 23, p. 183–222.

Doyle, M.G., and Huston, D.L., 1999, The subsea-floor replacement origin of the Ordovician Highway-Reward volcanic-associated massive sulfide deposit, Mount Windsor subprovince, Australia: Economic Geology, v. 94, p. 825–844.

Franklin, J.M., Lydon, J.W., and Sangster, D.F., 1981, Volcanic-associated massive sulfide deposits: Economic Geology, 75th Anniversary Volume, p. 485–627.

Franklin, J.M., Gibson, H.L., Jonasson, I.R., and Galley, A.G., 2005, Volcanogenic massive sulfide deposits: Economic Geology, 100th Anniversary Volume, p. 523–560.

Gabrielse, H., Murphy, D.C., and Mortensen, J.K., 2006, Cretaceous and Cenozoic dextral orogen-parallel displacements, magmatism, and paleogeography, north-central Canadian Cordillera: Geological Association of Canada, Special Paper 46, p. 255–276.

Gemmell, J.B., and Fulton, R., 2001, Geology, genesis, and exploration implications of the footwall and hanging-wall alteration associated with the Hellyer volcanic-hosted massive sulfide deposit, Tasmania, Australia: Economic Geology, v. 96, p. 1003–1035.

Gemmell, J.B., and Large, R.R., 1992, Stringer system and alteration zones underlying the Hellyer volcanic-hosted massive sulfide deposit, Tasmania, Australia: Economic Geology, v. 87, p. 620–649.

Genna, D., and Gaboury, D., 2015, Deciphering the hydrothermal evolution of a VMS system by LA-ICP-MS using trace elements in pyrite: An example

from the Bracemac-McLeod deposits, Abitibi, Canada, and implications for exploration: Economic Geology, v. 110, p. 2087–2108.

——2019, Use of semi-volatile metals as a new vectoring tool for VMS exploration: Example from the Zn-rich McLeod deposit, Abitibi, Canada Bracemac: Journal of Geochemical Exploration, v. 207, article 106358.

Genna, D., Gaboury, D., and Roy, G., 2014, The Key tuffite, Matagami camp, Abitibi greenstone belt, Canada: Petrogenesis and implications for VMS formation and exploration: Mineralium Deposita, v. 49, p. 489–512.

Gibson, H.L., Morton, R.L., and Hudak, G.J., 1999, Submarine volcanic processes, deposits, and environments favourable for the location of volcanic-associated massive sulfide deposits: Reviews in Economic Geology, v. 8, p. 15–51.

Gibson, H.L., Allen, R.L., Riverin, G., and Lane, T.E., 2007, The VMS model: Advances and application to exploration targeting: Decennial Mineral Exploration Conferences (DMEC), Decennial International Conference on Mineral Exploration, 5th, Toronto, Canada, Proceedings, p. 713–730.

Gifkins, C.C., and Allen, R.L., 2001, Textural and chemical characteristics of diagenetic and hydrothermal alteration in glassy volcanic rocks: Examples from the Mount Read volcanics, Tasmania: Economic Geology, v. 96, p. 973–1002.

Hannington, M.D., Kjarsgaard, I.M., Galley, A.G., and Taylor, B., 2003, Mineral-chemical studies of metamorphosed hydrothermal alteration in the Kristineberg volcanogenic massive sulfide district, Sweden: Mineralium Deposita, v. 38, p. 423–442.

Hannington, M.D., De Ronde, C.E.J., and Petersen, S., 2005, Sea-floor tectonics and submarine hydrothermal systems: Economic Geology, 100th Anniversary Volume, p. 111–141.

Herrmann, W., Blake, M., Doyle, M.G., Huston, D.L., Kamprad, J., Merry, N., and Pontual, S., 2001, Short wavelength infrared (SWIR) spectral analysis of hydrothermal alteration zones associated with base metal sulfide deposits at Rosebery and Western Tharsis, Tasmania, and Highway-Reward, Queensland: Economic Geology, v. 96, p. 939–955.

Hey, M.H., 1954, A new review of the chlorites: Mineralogical Magazine, v. 30, p. 277–292.

Holk, G.J., Taylor, B.E., and Galley, A.G., 2008, Oxygen isotope mapping of the Archean Sturgeon Lake caldera complex and VMS-related hydrothermal system, Northwestern Ontario, Canada: Mineralium Deposita, v. 43, p. 623–640.

Iijima, A., 1974, Clay and zeolite alteration zones surrounding Kuroko deposits in the Hokuroku district, Northern Akita, as submarine hydrothermal-diagenetic alteration products: Mining Geology, Special Issue no. 6, p. 267–289.

Jones, S., Herrmann, W., and Gemmell, J.B., 2005, Short wavelength infrared spectral characteristics of the HW horizon: Implications for exploration in the Myra Falls volcanic-hosted massive sulfide camp, Vancouver Island, British Columbia, Canada: Economic Geology, v. 100, p. 273–294.

Knuckey, M.J., Comba, C.D.A., and Riverin, G., 1983, Structure, metal zoning and alteration at the Millenbach deposit, Noranda, Quebec: Geological Association of Canada, Special Paper 25, p. 255–295.

Kranidiotis, P., and MacLean, W.H., 1987, Systematics of chlorite alteration at the Phelps Dodge massive sulfide deposit, Matagami, Quebec: Economic Geology, v. 82, p. 1898–1911.

Lafrance, B., Gibson, H.L., and Stewart, M.S., 2020, Internal and external deformation and modification of volcanogenic massive sulfide deposits: Reviews in Economic Geology, v. 21, p. 147–171.

Large, R.R., Allen, R.L., Blake, M.D., and Herrmann, W., 2001a, Hydrothermal alteration and volatile element halos for the Rosebery K lens volcanic-hosted massive sulfide deposit, western Tasmania: Economic Geology, v. 96, p. 1055–1072.

Large, R.R., Gemmell, J.B., Paulick, H., and Huston, D.L., 2001b, The alternation box plot: A simple approach to understanding the relationship between alteration mineralogy and lithogeochemistry associated with volcanic-hosted massive sulfide deposits: Economic Geology, v. 96, p. 957–971.

Large, R.R., McPhie, J., Gemmell, J.B., Herrmann, W., and Davidson, G.J., 2001c, The spectrum of ore deposit types, volcanic environments, alteration halos, and related exploration vectors in submarine volcanic successions: Some examples from Australia: Economic Geology, v. 96, p. 913–938.

Lentz, D.R., Hall, D.C., and Hoy, L.D., 1997, Chemostratigraphic, alteration, and oxygen isotopic trends in a profile through the stratigraphic sequence hosting the Heath Steele B zone massive sulfide deposit, New Brunswick: Canadian Mineralogist, v. 35, p. 841–874.

MacLean, W.H., 1988, Rare earth element mobility at constant inter-REE ratios in the alteration zone at the Phelps Dodge massive sulphide deposit, Matagami, Quebec: Mineralium Deposita, v. 23, p. 231–238.

——1990, Mass change calcualtions in altered rock series: Mineralium Deposita, v. 25, p. 44–49.

MacLean, W.H., and Barrett, T.J., 1993, Lithogeochemical techniques using immobile elements: Journal of Geochemical Exploration, v. 48, p. 109–133.

Magnall, J.M., Gleeson, S.A., Creaser, R.A., Paradis, S., Glodny, J., and Kyle, J.R., 2020, The mineralogical evolution of the clastic dominant-type Zn-Pb ± Ba deposits at Macmillan Pass (Yukon, Canada)—Tracing subseafloor barite replacement in the layered mineralization: Economic Geology, v. 115, p. 961–979.

Manor, M.J., and Piercey, S.J., 2018, Re-evaluating the chronostratigraphic framework for felsic volcanic and intrusive rocks of the Finlayson Lake region, Yukon-Tanana terrane, Yukon, *in* MacFarlane, K.E., ed., Yukon Exploration and Geology 2017: Yukon Geological Survey, p. 111–127.

——2019, Geochemistry of Devono-Mississippian volcanic and intrusive rocks of the Finlayson Lake district, Yukon-Tanana terrane, Yukon, *in* MacFarlane, K.E., ed., Yukon Exploration and Geology: Yukon Geological Survey, p. 91–110.

Manor, M. J., Piercey, S. J., Murphy, D. C., and Wall, C. J., 2022a, Age and Chemostratigraphy of the Finlayson Lake District , Yukon: Implications for Volcanogenic Massive Sulfide (VMS) Mineralization and Tectonics along the Western Laurentian Continental Margin: Lithosphere, v. 2022, p. 45.

Manor, M.J., Piercey, S.J., Wall, C.J., and Denisová, N., 2022b, High precision CA-ID-TIMS U-Pb zircon geochronology of felsic rocks in the Finlayson Lake VMS district, Yukon: Linking Paleozoic basin-scale accumulation rates to the occurrence of subseafloor replacement-style mineralization: Economic Geology, v. 117, p. 1173–1201.

Mathieu, L., 2018, Quantifying hydrothermal alteration: A review of methods: Geosciences, v. 8, 27 p.

McNulty, B.A., Fox, N., and Gemmell, J.B., 2020, Assessing hydrothermal alteration intensity in volcanic-hosted massive sulfide systems using portable X-ray fluorescence analysis of drill core: An example from Myra Falls, Canada: Economic Geology, v. 115, p. 443–453.

Mercier-Langevin, P., Lafrance, B., Bécu, V., Dubé, B., Kjarsgaard, I., and Guha, J., 2014, The Lemoine auriferous volcanogenic massive sulfide deposit, Chibougamau camp, Abitibi greenstone belt, Quebec, Canada: Geology and genesis: Economic Geology, v. 109, p. 231–269.

Mortensen, J.K., 1992, Pre-mid-Mesozoic tectonic evolution of the Yukon-Tanana terrane, Yukon and Alaska: Tectonics, v. 11, p. 836–853.

Mortensen, J.K., and Jilson, G.A., 1985, Evolution of the Yukon-Tanana terrane: Evidence from southeastern Yukon territory: Geology, v. 13, p. 806–810.

Munhá, J., Fyfe, W.S., and Kerrich, R., 1980, Adularia, the characteristic mineral of felsic spilites: Contributions to Mineralogy and Petrology, v. 75, p. 15–19.

Murphy, D.C., and Piercey, S.J., 1998, Finlayson project: Geological evolution of Yukon-Tanana terrane and its relationship to Campbell Range belt, northern Wolverine Lake map area, southeastern Yukon, *in* Roots, C.F., and Emond, D.S., eds., Yukon exploration and geology: Yukon Geological Survey p. 47–62.

Murphy, D. C., Mortensen, J. K., Piercey, S. J., Orchard, M. J., and Gehrels, G. E., 2006, Mid-Paleozoic to early Mesozoic tectonostratigraphic evolution of Yukon-Tanana and Slide Mountain terranes and affiliated overlap assemblages, Finlayson Lake massive sulphide district, southeastern Yukon: Geological Association of Canada, Special Paper 45, p. 75–106.

Nelson, J.L., Piercey, S.J., Murphy, D.C., Colpron, M., Dusel-Bacon, C., and Roots, C.F., 2006, Paleozoic tectonic and metallogenetic evolution of pericratonic terranes in Yukon, northern British Columbia and eastern Alaska: Geological Association of Canada, Special Paper 45, p. 323–360.

Nozaki, T., Nagase, T., Takaya, Y., Yamasaki, T., and Otake, T., 2021, Subseafloor sulphide deposit formed by pumice replacement mineralisation: Scientific Reports, v. 11, p. 1–11.

van Olden, K., Green, A., and Davidson, G., 2020, NI 43-101 feasibility study technical report, Kudz Ze Kayah property, Yukon, Canada: CSA Global, Report no. R173.2019, 376 p.

Peter, J.M., Layton-Matthews, D., Piercey, S.J., Bradshaw, G.D., Paradis, S., and Bolton, A., 2007, Volcanogenic-hosted massive sulphide deposits of the Finlayson Lake district, Yukon: Geological Association of Canada, Mineral Deposits Division, Special Publication 5, p. 471–508.

Piercey, S.J., 2015, A semipermeable interface model for the genesis of subseafloor replacement-type volcanogenic massive sulfide (VMS) deposits: Economic Geology, v. 110, p. 1655–1660.
Piercey, S.J., and Colpron, M., 2009, Composition and provenance of the Snowcap assemblage, basement to the Yukon-Tanana terrane, northern Cordillera: Implications for Cordilleran crustal growth: Geosphere, v. 5, p. 439–464.
Piercey, S.J., Murphy, D.C., Mortensen, J.K., and Paradis, S., 2001a, Boninitic magmatism in a continental margin setting, Yukon-Tanana terrane, southeastern Yukon, Canada: Geology, v. 29, p. 731–734.
Piercey, S.J., Paradis, S., Murphy, D.C., and Mortensen, J.K., 2001b, Geochemistry and paleotectonic setting of felsic volcanic rocks in the Finlayson Lake volcanic-hosted massive sulfide district, Yukon, Canada: Economic Geology, v. 96, p. 1877–1905.
Piercey, S.J., Mortensen, J.K., Murphy, D.C., Paradis, S., and Creaser, R.A., 2002, Geochemistry and tectonic significance of alkalic mafic magmatism in the Yukon-Tanana terrane, Finlayson Lake region, Yukon: Canadian Journal of Earth Sciences, v. 39, p. 1729–1744.
Piercey, S.J., Mortensen, J.K., and Creaser, R.A., 2003, Neodymium isotope geochemistry of felsic volcanic and intrusive rocks from the Yukon-Tanana terrane in the Finlayson Lake region, Yukon, Canada: Canadian Journal of Earth Sciences, v. 40, p. 77–97.
Piercey, S.J., Nelson, J.L., Colpron, M., Dusel-Bacon, C., Simard, R.-L.L., and Roots, C.F., 2006, Paleozoic magmatism and crustal recycling along the ancient Pacific margin of North America, northern Cordillera: Geological Association of Canada, Special Paper 45, p. 281–322.
Piercey, S.J., Squires, G.C., and Brace, T.D., 2014, Lithostratigraphic, hydrothermal, and tectonic setting of the Boundary volcanogenic massive sulfide deposit, Newfoundland Appalachians, Canada: Formation by subseafloor replacement in a Cambrian rifted arc: Economic Geology, v. 109, p. 661–687.
Piercey, S.J., Gibson, H.L., Tardif, N., and Kamber, B.S., 2016, Ambient redox and hydrothermal environment of the Wolverine volcanogenic massive sulfide deposit, Yukon: Insights from lithofacies and lithogeochemistry of Mississippian host shales: Economic Geology, v. 111, p. 1439–1463.
Pilote, J.L., Piercey, S.J., and Mercier-Langevin, P., 2019, Evolution of the subseafloor hydrothermal system associated with the Ming VMS deposit, Newfoundland Appalachians, and its controls on base and precious metal distribution: Mineralium Deposita, v. 55, p. 913–936.
Reimann, C., Filzmoser, P., and Garrett, R.G., 2005, Background and threshold: Critical comparison of methods of determination: Science of the Total Environment, v. 346, p. 1–16.
Richards, H.G., Cann, J.R., and Jensenius, J., 1989, Mineralogical zonation and metasomatism of the alteration pipes of Cyprus sulfide deposits: Economic Geology, v. 84, p. 91–115.
Riverin, G., and Hodgson, C.J., 1980, Wall-rock alteration at the Millenbach Cu-Zn mine, Noranda, Quebec: Economic Geology, v. 75, p. 424–444.
Ruks, T.W., Piercey, S.J., Road, L., Pe, O., Ryan, J.J., Villeneuve, M.E., and Creaser, R.A., 2006, Mid- to late Paleozoic K-feldspar augen granitoids of the Yukon-Tanana terrane, Yukon, Canada: Implications for crustal growth and tectonic evolution of the northern Cordillera: Geological Society of America Bulletin, v. 118, p. 1212–1231.
Saccocia, P.J., and Seyfried, W.E., 1994, The solubility of chlorite solid solutions in 3.2 wt % NaCl fluids from 300-400°C, 500 bars: Geochimica et Cosmochimica Acta, v. 58, p. 567–585.
Sangster, D.F., 1980, Quantitative characteristics of volcanogenic massive sulphide deposits - Metal content and size distribution of massive sulphide deposits in volcanic centers: Canadian Institute of Mining, Metallurgy and Petroleum (CIM) Bulletin, v. 73, p. 74–81.
Schardt, C., Cooke, D.R., Gemmell, J.B., and Large, R.R., 2001, Geochemical modeling of the zoned footwall alteration pipe, Hellyer volcanic-hosted massive sulfide deposit, Western Tasmania, Australia: Economic Geology, v. 96, p. 1037–1054.
Sebert, C., Hunt, J.A., and Foreman, I.J., 2004, Geology and lithogeochemistry of the Fyre Lake copper-cobalt-gold sulphide-magnetite deposit, southeastern Yukon: Yukon Geological Survey, Open File 2004-17, 46 p.
Soltani Dehnavi, A., Lentz, D.R., McFarlane, C.R.M., and Walker, J.A., 2018b, Quantification of fluid-mobile elements in white mica by LA-ICP-MS: From chemical composition to a potential micro-chemical vectoring tool in VMS exploration: Journal of Geochemical Exploration, v. 188, p. 290–307.
Soltani Dehnavi, A., McFarlane, C.R.M., Lentz, D.R., McClenaghan, S.H., Walker, J.A., Dehnavi, A.S., McFarlane, C.R.M., Lentz, D.R., McClenaghan, S.H., and Walker, J.A., 2019, Chlorite-white mica pairs' composition as a micro-chemical guide to fingerprint massive sulfide deposits of the Bathurst mining camp, Canada: Minerals, v. 9, 31 p.
Spitz, G., and Darling, R., 1978, Major and minor element lithogeochemical anomalies surrounding the Louvem copper deposit, Val d'Or, Quebec: Canadian Journal of Earth Sciences, v. 15, p. 1161–1169.
Urabe, T., Scott, S.D., and Hattori, K., 1983, A comparison of footwall-rock alteration and geothermal systems beneath some Japanese and Canadian volcanogenic massive sulfide deposits: Economic Geology Monograph 5, p. 345–364.
Velde, B., 1978, Infrared spectra of synthetic micas in the series muscovite-MgAl celadonite: American Journal of Science, v. 63, p. 343–349.
Yang, K., Huntington, J.F., Gemmell, J.B., and Scott, K.M., 2011, Variations in composition and abundance of white mica in the hydrothermal alteration system at Hellyer, Tasmania, as revealed by infrared reflectance spectroscopy: Journal of Geochemical Exploration, v. 108, p. 143–156.
Zang, W., and Fyfe, W.S., 1995, Chloritization of the hydrothermally altered bedrock at the Igarapé Bahia gold deposit, Carajás, Brazil: Mineralium Deposita, v. 30, p. 30–38.

Nikola Denisová is a Ph.D. candidate at Memorial University of Newfoundland. Her project focuses on the genesis of the ABM replacement-style VMS deposit, Yukon, Canada. Nikola received her B.Sc. in geology from Charles University in Prague and her M.Sc. in geosciences at Luleå University of Technology. Prior to starting on her Ph.D. program in Canada, Nikola worked in iron, nickel, and gold exploration and mining projects in northern Sweden for 4.5 years.